Article

Quantitative Analysis and Modeling Probe Polarity Establishment in *C. elegans* Embryos

Simon Blanchoud,[1,2] Coralie Busso,[1] Félix Naef,[2] and Pierre Gönczy[1,*]
[1]Swiss Institute for Experimental Cancer Research (ISREC) and [2]The Institute of Bioengineering (IBI), School of Life Sciences, Swiss Federal Institute of Technology (EPFL), Lausanne, Switzerland

ABSTRACT Cell polarity underlies many aspects of metazoan development and homeostasis, and relies notably on a set of PAR proteins located at the cell cortex. How these proteins interact in space and time remains incompletely understood. We performed a quantitative assessment of polarity establishment in one-cell stage *Caenorhabditis elegans* embryos by combining time-lapse microscopy and image analysis. We used our extensive data set to challenge and further specify an extant mathematical model. Using likelihood-based calibration, we uncovered that cooperativity is required for both anterior and posterior PAR complexes. Moreover, we analyzed the dependence of polarity establishment on changes in size or temperature. The observed robustness of PAR domain dimensions in embryos of different sizes is in agreement with a model incorporating fixed protein concentrations and variations in embryo surface/volume ratio. In addition, we quantified the dynamics of polarity establishment over most of the viable temperatures range of *C. elegans*. Modeling of these data suggests that diffusion of PAR proteins is the process most affected by temperature changes, although cortical flows appear unaffected. Overall, our quantitative analytical framework provides insights into the dynamics of polarity establishment in a developing system.

INTRODUCTION

A widespread mechanism to polarize cells in metazoan organisms relies on generating spatially restricted domains of protein enrichment at the cell cortex below the plasma membrane. Such cortical polarization is important for many aspects of cellular behavior and development, including asymmetric cell division, cell migration, and determination of body axes (reviewed in (1)). Defects in cortical cell polarity have been associated with a variety of disease conditions, including cancer (reviewed in (2)).

The core molecular players of cortical polarity were identified in the nematode *Caenorhabditis elegans*, where their inactivation results in PARtitioning defective phenotypes characterized by impaired asymmetric cell division (3). In the wild-type (WT) ~50 μm-long *C. elegans* embryo, cortical polarity is established during the first cell cycle, thereby defining the anterior-posterior embryonic axis. Initially, the so-called anterior PAR complex, consisted of PAR-3, PAR-6, and PKC-3, occupies the entire cortex in a uniform manner, whereas the posterior components PAR-2, PAR-1, and LGL-1 are cytoplasmic (reviewed in (4)). The actomyosin network, a central constituent of the cell cortex, is uniformly tensed at this stage. Shortly thereafter, symmetry is broken in the vicinity of the centrosomes through a local reduction in cortical tension at the presumptive posterior pole (5–7). This initiates an anterior-directed cortical flow that promotes clearance of the anterior PAR complex from the posterior side, as well as binding of PAR-2, PAR-1, and LGL-1 to the thus depleted region of the posterior cortex (8,9). Thereupon, the first phase of polarity establishment (hereafter referred to as initiation) continues for ~5 min through retraction of the anterior domain and concomitant expansion of the posterior domain until the two each occupy approximately half of the embryo cortex (8). The second phase of polarity establishment (hereafter referred to as maintenance) follows, during which the anterior and posterior domains remain stationary for ~10 min until the first mitotic division takes place.

Polarization in one-cell stage *C. elegans* embryos relies on the mutual inhibition between the anterior and the posterior PAR proteins, leading to the formation of two nonoverlapping cortical domains (10,11). Such mutual inhibition and, more generally, polarity establishment, have been the subjects of mathematical models that capture the essence of the underlying molecular interactions (12–14). Although several parameters characterizing these processes were measured experimentally (15), the parameters governing mutual inhibition were assigned empirically to enable modeling (13), leaving uncertainties concerning the underlying mechanism. Regardless of the mathematical model, polarity establishment must be robust to changes in size and temperature. *C. elegans* embryos that are ~30 μm- to ~75 μm-long are viable and give rise to fertile adults (16,17). Therefore, scaling of the PAR domains must take place, although the extent to which this is the case

Submitted June 19, 2014, and accepted for publication December 11, 2014.
*Correspondence: pierre.gonczy@epfl.ch
Editor: Stanislav Shvartsman.

0006-3495/15/02/0799/11 $2.00
http://dx.doi.org/10.1016/j.bpj.2014.12.022

has not been investigated. Moreover, because *C. elegans* can develop between ~10°C and ~25°C (18), polarization must also tolerate temperature variations, but how this occurs has not been investigated either. Here, we address these and related outstanding issues by combining quantitative microscopy with mathematical modeling, thus yielding important insights into polarity establishment dynamics in *C. elegans* embryos.

MATERIALS AND METHODS

Worm strains, cell cycle timing, and RNAi

All *C. elegans* strains were maintained at 24°C according to standard procedures (19). For recordings performed at 20°C and 13°C, the strains were shifted to a lower temperature at least 1 h before imaging. The transgenic strain expressing green fluorescent protein (GFP) fusion proteins were kindly provided as follows: mCherry::PH (OD70 (20)) by Karen Oegema, GFP::PAR-2(RNAi resistant); *par- 2(ok1723)* animals (JH2951 (21)) by Fumio Motegi, GFP::PAR-2(RNAi resistant) (TH129 (22)) by Anthony Hyman, GFP::PAR-2 (KK866 (8)) by Kenneth Kemphues, and VIT-2::GFP (RT130 (23)) by the *Caenorhabditis* Genetics Center.

Determination of three key events during the first cell cycle was performed by visual inspection of the recordings and their timing defined as follows: pseudocleavage furrow, maximal ingression of the pseudocleavage furrow; pronuclear meeting, first contact between pronuclei; cytokinesis, cleavage furrow initiation.

The bacterial RNAi feeding strain for *C27D9.1* was obtained from the *C. elegans* ORFeome RNAi library (gift from Jean-François Rual and Marc Vidal, Harvard Medical School, Boston, MA). The bacterial RNAi feeding strain for *ani-2* was obtained from the Ahringer RNAi library (24). Bacteria were prepared as described (25) and fed to starved L1 animals for 48 h at 24°C.

Time-lapse microscopy and temperature control

GFP::PAR-2(RNAi resistant); *par-2(ok1723)*; mCherry-PH (GZ1056) nematodes were dissected in tempered osmotically balanced blastomere culture medium (26). Embryos were imaged using multichannel time-lapse differential interference contrast (DIC) and fluorescence microscopy on a Zeiss Axioplan 2 with a 63× oil objective and a 6% neutral density filter to attenuate the 103 W Arc Mercury epifluorescent source. The microscope and the 1392 × 1040 pixels 12-bit Photometrics CoolSNAP ES2 camera were controlled by μManager (27). Images were taken every 10 s with the following exposure time: DIC, 100 ms; GFP, 500 ms; mCherry, 250 ms. The focus was manually adjusted during the recordings to remain close to the mid-embryo focal plane.

For WT recordings, an additional Fast response temperature control unit (GP205, EMBL (28)) was used to obtain very stable temperature conditions. The samples were mounted as detailed by the manufacturer on 22 × 40 × 0.14 mm coverslips and the stage filled with desalted water. To obtain an optimal DIC image despite the copper grid present 1 mm below the slide, an achromatic condenser head P 0.90 S1 from Leica was adapted to the Zeiss Axioplan 2.

Otherwise WT VIT-2::GFP worms were prepared similarly but imaged on a PerkinElmer Spinning-Disk Confocal equipped with a 60× oil objective and an 488 nm Argon laser. Images were taken every second on a Hamamatsu EMCCD C9100-50 camera with an exposure time of 250 ms. The focus was manually adjusted during the recordings to keep the imaging plane focused on the male pronucleus. VIT-2::GFP *ani-2(RNAi)* and VIT-2::GFP *C27D9.1(RNAi)* embryos were imaged in a similar manner but on a Yokogawa Spinning-Disk CSU-W1 equipped with a 60× oil objective and a Hamamatsu EMCCD ImagEM B/W camera.

All recordings were performed under controlled temperature conditions. *ani-2(RNAi)* and *C27D9.1(RNAi)* recordings were acquired in an air-conditioned room at 23°C, VIT-2::GFP in another room kept at 22°C.

RESULTS

Monitoring polarity establishment

To challenge and potentially improve extant mathematical models, we performed multichannel time-lapse recordings of polarity establishment in 140 embryos, monitoring the posterior cortical domain with GFP::PAR-2 at a frame rate of 0.1 Hz (Fig. S1, *A–C*, in the Supporting Material; Movie S1; Materials and Methods). To avoid nonphysiological levels of PAR-2, we used a strain expressing GFP::PAR-2 (21) in a *par-2(ok1723)* deletion mutant background to remove endogenous PAR-2. These worms are fully viable and fertile, attesting to the functionality of the fusion protein. In addition, immunofluorescence analysis showed that cortical PAR-2 levels in this strain are closer to the WT than in a previously used strain expressing GFP::PAR-2 on top of endogenous PAR-2 (13) (Fig. S1, *D–F*). We crossed the newly obtained worms with transgenic animals expressing mCherry::PH (20) to visualize the plasma membrane in the entire embryo and acquired a collection of high spatial and temporal data sets including five recording conditions (Fig. S1 *G*). This provides a unique resource for a quantitative study of polarity establishment, including upon size or temperature perturbations.

Quantifying polarity establishment

To precisely measure polarity establishment in every embryo, we combined ASSET (29), a fully automated segmentation and standardization algorithm, with a signal quantification method developed specifically for this study (see the Supporting Material). ASSET first identifies the embryo eggshell in the DIC channel (Fig. 1 *A*) and then locates the cell membrane using the mCherry::PH signal (Fig. 1 *B*). Thereafter, the DIC and mCherry::PH segmentations are smoothed and used to guide GFP::PAR-2 signal detection (Fig. 1, *C* and *D*). The signal intensity along the membrane (Fig. 1 *E*) is then quantified after separation from the cytoplasmic signal, from the eggshell autofluorescence and from the noise (Fig. S1, *H–M*). The GFP::PAR-2 cortical signal was thus determined for every frame, yielding a high-resolution kymograph of polarity establishment represented in absolute distance (Fig. 1 *F*).

During polarity establishment, a process referred to as posteriorization centers the growing posterior domain to the closest pole of the embryo (30,31). Because we focused this study on the expansion of the posterior domain, we normalized for posteriorization by automatically detecting the center and the extent of the expanding GFP::PAR-2 domain in the kymographs (Fig. 1, *F* and *G*, and Supporting Material). Together, the previous steps enabled us to

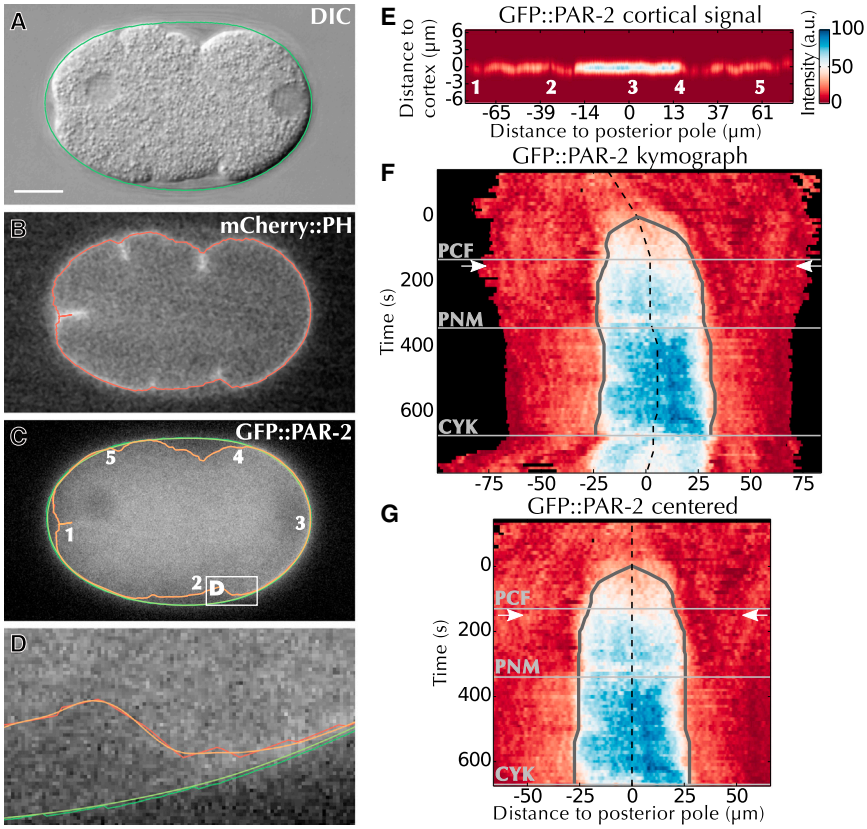

FIGURE 1 Quantifying polarity establishment. (*A–D*) Automated segmentation using ASSET. ASSET first (*A*) identifies the eggshell (*green*) in the DIC image, and then (*B*) segments the cell membrane (*red*) in the mCherry::PH image, and finally (*C*) transposes these two segmentations (*green and red*) to the GFP::PAR-2 channel and smoothes them (*light green and orange*). The white box delimits the area magnified in (*D*). Numbers in (*C*) and (*E*) denote corresponding locations. (*D*) Magnification of area delimited in (*C*) by the white box. (*E*) Perpendicular quantification of GFP::PAR-2 fluorescence in frame *C* (Fig. S1, *H–M*). (*F*) Kymograph of the recording containing the frame shown in (*A*)–(*C*) (see Movie S1), overlaid with automatic detection of the domain center (*dashed line*) and of domain expansion (*gray line*). Horizontal lines: cell cycle events (see Materials and Methods); arrows: position of the frame shown in (*A*)–(*E*). Black areas correspond to locations outside the embryo. (*G*) Final kymograph after centering and cropping, overlaid with landmarks as in (*F*). CYK, cytokinesis; PCF, pseudocleavage furrow; PNM, pronuclear meeting.To see this figure in color, go online.

robustly determine the dynamics of GFP::PAR-2 accumulation at the cell cortex in 140 embryos.

A model with newly measured cortical flows faithfully captures the experimental data

To quantitatively assess how the spatial and temporal dynamics of PAR-2 predicted from mathematical models matches our kymographs, we developed a likelihood score (Eq. S1 and the Supporting Material). The extant model we initially considered ((13), termed M1) is one-dimensional, assuming rotational symmetry along the longitudinal embryonic axis, and simulates the concentration of both anterior and posterior complexes at the cortex over space and time. This model accounts for binding and unbinding of the complexes to the cortex, protein diffusion within the cortex, and cortical flows, all of which have been determined experimentally (15). In addition, the model embeds mutual inhibition between the two complexes, which involves nonlinear interactions with cooperativity exponents α and β that have not been determined experimentally (Eq. S2, Eq. S3 and the Supporting Material).

To assess the performance of M1, the 47 WT recordings performed at 24°C were averaged after temporal registration to reduce variability between kymographs (Figs. 2 *A* and S2, *A* and *B*). The resulting average was in qualitative agreement with M1 using the published parameter values (Figs. 2 *B* and S2, *C* and *D*; Table S1 (13)). However, the salient leading edge enrichment and concomitant overshooting reported previously (13) was observed to a much lesser extent in our experiments (Fig. 2 *B*, *arrowheads*, compare with Fig. 2 *A*). We considered whether the more salient enrichment might result from the excess of total PAR-2 in the previous analysis (see Fig. S1 *E*). However, we found that simulating an excess of posterior versus anterior complexes still resulted in notable leading edge enrichment (Fig. S3, *A–C*). Therefore, we set out to investigate further what in the model may cause such discrepancy with the experimental results. In a first approach that minimizes the changes with respect to the original model M1, we tested whether individual parameters, including those that had been experimentally determined previously (15), needed to be adjusted (Fig. S3, *D–W*). However, none of the tested parameter variations could reduce the salient leading edge enrichment and the concomitant domain overshooting (Fig. S3). Given that the four parameters governing mutual inhibition between anterior and posterior components (i.e., k_{AP}, α, k_{PA}, and β) were not measured experimentally, we reasoned that re-optimizing all these four parameters simultaneously (into a model termed M1*) could reduce the discrepancies with the data. We found that, although this improved the simulation at the leading edge, the predicted initiation phase of polarity establishment was still not in agreement with the

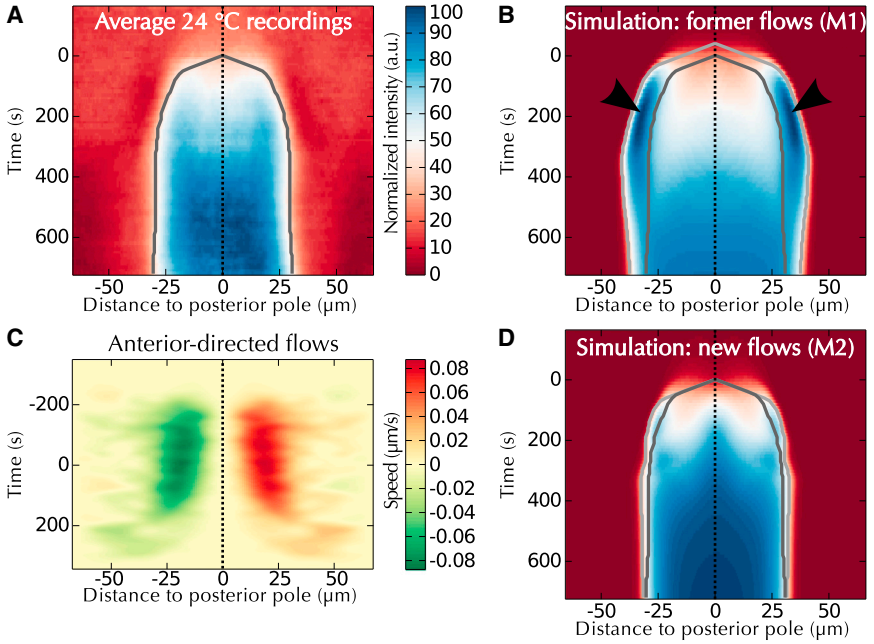

FIGURE 2 Model with newly measured cortical flows faithfully captures the experimental data. (*A*) Average GFP::PAR-2 protein distribution during polarity establishment at 24°C ($n = 47$), overlaid with segmentation of domain center (*dashed line*) and domain expansion (*dark gray*). Time zero in this figure: onset of polarity establishment, as identified by domain segmentation. (*B*) Polarity establishment as predicted by M1 (Table S1 (13)), overlaid with the segmentation of this prediction (*light gray*) and of our experimental data (*dark gray*). Arrowheads indicate leading front enrichment not observed in (*A*). (*C*) Cortical flows measured using VIT-2::GFP particle tracking (Fig. S4 and the Supporting Material). (*D*) Polarity establishment as predicted by M2 (i.e., M1 with flows shown in *C*), overlaid with landmarks similar to (*B*). Note the strong dampening of leading edge enrichment. To see this figure in color, go online.

experimental data (Fig. S2 *E*). We thus decided to explore whether another minimal modification to M1 could reduce this leading edge while keeping the model as close as possible to the published experimental parameter values. Because of the importance of cortical flows in the early dynamics of polarity establishment (9), and because the two-dimensional (2D) cortical flow velocity map accompanying M1 stems from only a few measurements (13), we considered whether this could be the source of the observed discrepancy.

We thus set out to estimate cortical flows anew. We used the movements of subcortical VIT-2::GFP yolk granules as a proxy (32), because we anticipated that the high number of granules that can be analyzed in this manner compared to the lower number of nonmuscle myosin (NMY-2) foci should generate a more accurate 2D cortical velocity map, in particular close to the site of polarity initiation (see the Supporting Material). This approach enabled us to detect ~450 particles per frame (i.e., over 1.7 million particles in total, Figs. S4 and S5). The resulting 2D velocity map (~0.08 μm/s at the maximal location, Fig. 2 *C*) is characterized by slightly slower flows than those stemming from previous measurements based on NMY-2::GFP (~0.11 μm/s on average, Table S2 (9,13,33)), while being analogous to earlier one-dimensional measurements based on manual tracking of individual yolk granules (~0.07 μm/s, Table S2 (34,35)) as well as with measurements performed using particle image velocimetry as an alternative means to quantify flows (Fig. S6 and (32)). Of importance, incorporating the newly determined 2D cortical flows into a revised version of the original mathematical model M1 (termed M2) drastically dampened the previously noted leading edge enrichment (Figs. 2 *D* and S2, *G* and *H*). Therefore, model M2 provides a more accurate quantitative description of polarity establishment in the WT.

Cooperativity of both anterior and posterior components is required to account for polarity establishment

Among the model parameters (Table S1 and Eqs. S2 and S3 in the Supporting Material), those governing mutual inhibition between anterior and posterior components (i.e., k_{AP}, α, k_{PA}, and β) do not rely on experimental measurements, but were chosen empirically to allow for a stable initial homogeneous anterior state and a stable final polarized state (13). Given that other combinations of values can give rise to such behaviors (13), we decided to use M2 to infer those four values from our data set. Because our data set provides data on the dynamics of the posterior domain and merely infers parameter values of the anterior domain, we set out to test whether such inferences are precise. To this end, we conducted simulation experiments using the same maximum-likelihood optimization procedure applied for the actual data, which demonstrated that the inferences derived for the anterior domain are indeed precise (Fig. S7, Eq. S1, and Supporting Material). We thus could identify the most likely values independently for each embryo (Fig. 3), and hence obtained the distribution of parameters that can give rise to polarity establishment (Fig. S8). Correlation analysis of the estimated parameters (Fig. S8 *O* (36)) confirmed the need for tightly coregulated mutual inhibition rates k_{AP} and k_{PA} (Fig. S8 *G*), as previously derived analytically (13), while revealing covariance between the other parameters of the mathematical model.

The average estimated values provided insights into the mutual inhibition process, both in terms of the rates and

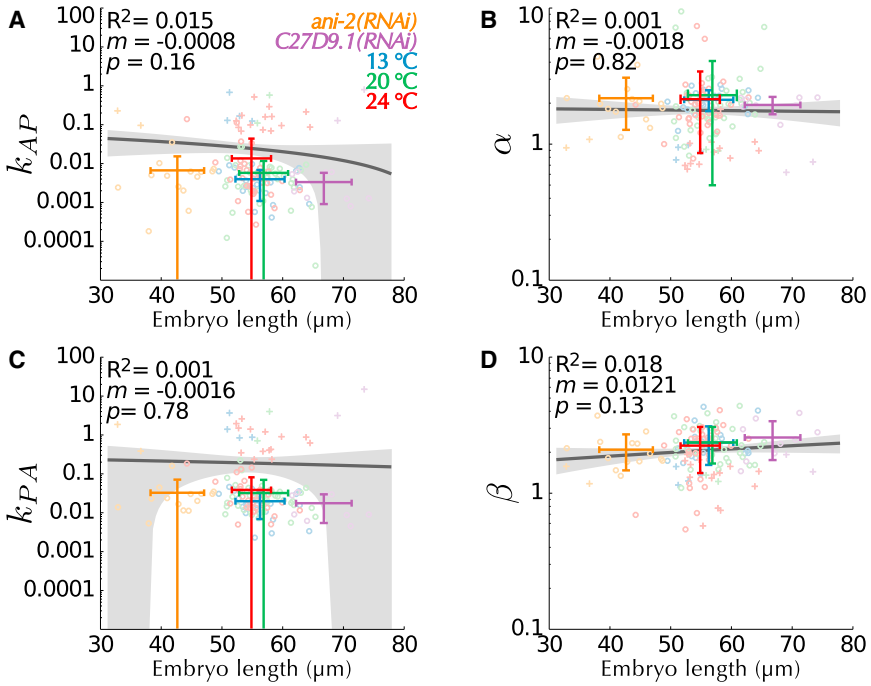

FIGURE 3 Cooperativity of both anterior and posterior components is required for polarity establishment. (*A–D*) Best values for the unmeasured mutual inhibition parameters {(*A*) k_{AP}, (*B*) α, (*C*) k_{PA}, (*D*) β} was identified in each embryo by an optimization procedure. Values detected as outliers (see the Supporting Material) are depicted using crosses and removed from the calculation of the mean as well as from the parameter distribution (Fig. S8). Values are color-coded with respect to their recording condition and overlaid with the corresponding average and standard deviation. Shown are the linear regression (*dark gray line*) with the corresponding 95% confidence interval (*light gray area*), the correlation coefficient R^2 that reports the fraction of variance explained by the linear regression, the slope of the correlation m and the p-value (Student's two-tailed t-test for the coefficient m). To see this figure in color, go online.

cooperativity exponents. First, the two mutual inhibition rates were significantly smaller than the formerly proposed values ($k_{AP} = 0.008 \pm 0.017$ and $k_{PA} = 0.030 \pm 0.035$ compared to 0.19 and 2, respectively, Fig. 3, *A* and *C*, and Table S3 (13), all $\pm$ represent standard deviations). Such smaller rates reflect reduced mutual inhibition and are required to account for the low GFP::PAR-2 signal on the anterior half (Fig. S2, *I* and *K*, *lighter red*, compared to Fig. S2, *C* and *G*, *dark red*). Second, our analysis revealed a difference in the value of one of the exponents compared to that previously chosen. α describes the cooperative action of posterior proteins toward inhibiting the anterior complex, and vice-versa for β (see the Supporting Material). Values >1 for α or β indicate nonlinear biochemical kinetics such as oligomerization (37) or multisite phosphorylation (38). Our data confirms that the hypothesized cooperativity for the anterior complex ($\beta = 2$ in (13,14)) is necessary to explain the data ($\beta = 2.30 \pm 0.74$, Fig. 3 *D*). In addition and of importance, in contrast to previous conclusions ($\alpha = 1$ in (12–14)), our results predict that cooperativity in the posterior domain is also required ($\alpha = 2.17 \pm 1.28$, Fig. 3 *B*). This suggests a nonlinear mechanism involved in the exclusion by posterior proteins of the anterior complex.

Fixed protein concentration combined with changes in surface/volume ratio underlies domain scaling

We next investigated how polarity can be established seemingly normally over a wide range of embryo sizes (16,17). Here, we define perfect scaling as a situation where the relative size of the posterior domain is independent of embryo size. To probe the degree to which scaling operates in vivo, we quantified the extent of the posterior domain in smaller embryos generated using RNA-interference (RNAi)-mediated depletion of the anillin gene *ani-2* ($n = 16$, Fig. 4, *A* and *B* (16)), in WT embryos ($n = 47$, Fig. 4, *C* and *D*), as well as in larger embryos generated using RNAi-mediated depletion of the open reading frame *C27D9.1* ($n = 11$, Fig. 4, *E* and *F* (39)). We found that the size of the posterior domain scaled with membrane length, albeit not perfectly (Fig. S9 *A*).

We next studied whether the mathematical model could reproduce such behavior. Scaling is anticipated from the model because the size of the posterior domain is governed mathematically by the relative abundance of anterior versus posterior proteins (13), which should be independent from cell size given that oocytes derive from a common syncytium. To assess the actual degree of scaling in the model, we simulated M2 with the estimated parameters for mutual inhibition (see Fig. 3). M2 indeed predicts that domain length increases with membrane length (Fig. S9 *C*). However, scaling is imperfect, with smaller embryos showing proportionally larger posterior domains (Fig. S9 *D*), as anticipated because the surface/volume ratio φ, which decreases for larger cells (see the Supporting Material), dictates the protein pool available to bind the membrane (Eq. S3 in the Supporting Material).

Intriguingly, the scaling observed experimentally is even less precise than the model predictions (Fig. S9 *B*, compare with Fig. S9 *D*), raising the possibility that the model does not capture the full impact of cell size on polarity establishment. One process that may contribute further to size

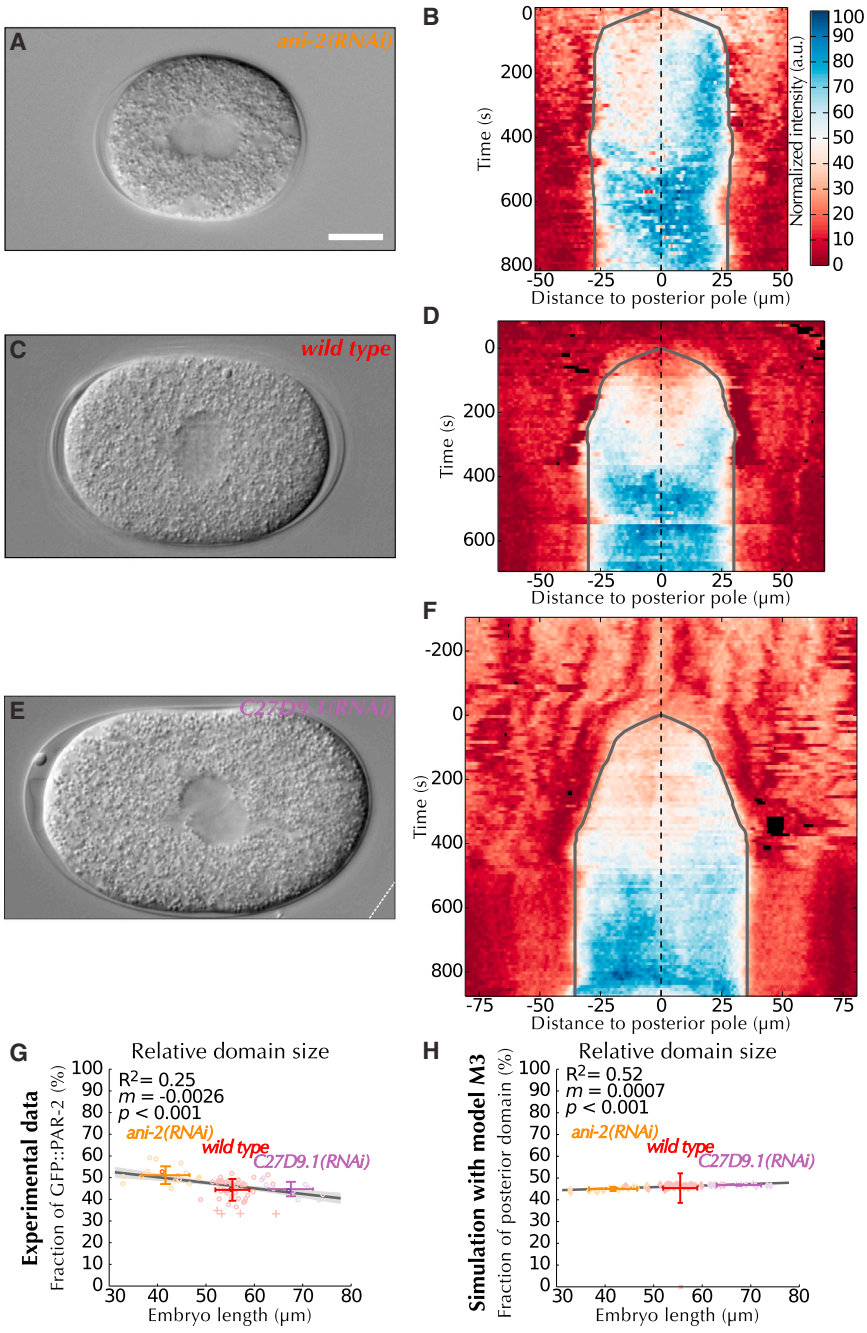

FIGURE 4 Fixed protein concentration and changes in surface/volume ratio underlie domain scaling. (*A*, *C*, and *E*) DIC images representing the median embryo of each recording condition and (*B*, *D*, and *F*) corresponding kymographs, overlaid with landmarks similar to Fig. 1. The white dashed line in *E* delimits the boundary of the raw image. (*G*) Linear regression (*dark gray line*) performed on the length of the embryo versus the fraction of the membrane spanned by GFP::PAR-2, overlaid with landmarks similar to Fig. 3. The darker circles indicate the locations of the median recordings depicted in (*A*)–(*F*). (*H*) Same as (*G*), but quantifying the extent of the posterior domain as predicted by M3 (i.e., using the values calibrated with the median recordings). To see this figure in color, go online.

dependence is cortical flow. Indeed, extending the assumption of fixed protein concentrations to components of the actomyosin cytoskeleton, we deduced that the magnitude of cortical flows could be inversely proportional to φ (see the Supporting Material). To test this hypothesis, we determined cortical flows both in smaller *ani-2(RNAi)* ($n = 6$) and larger *C27D9.1(RNAi)* embryos ($n = 8$), which were analyzed in conjunction with cortical flows in the WT. As shown in Fig. S9, *E* and *F*, we did not observe a correlation between cortical flows and either embryo length, or surface/volume ratio. Therefore, because we sought to derive a single model able to capture the entire data set, we explored whether some of the unmeasured parameters would need to be optimized. We thus recalibrated the model (i.e., optimized k_{AP}, α, k_{PA}, and β) using together the median embryo from the small, normal and large data sets (Fig. 4 *G* and Supporting Material). Although the resulting model (M3, Table S3) matches the experimentally measured domain length using a single set of parameter values (Fig. S9 *G*), it does not fully capture the correlation between embryo length and relative domain size (Fig. 4 *H*). This suggests that an additional mechanism involved in domain scaling has not been

incorporated into the model. Irrespective of these small variations, the four mutual inhibition parameters in M3 were similar to those obtained with M2 (Table S3), reinforcing our conclusion that cooperativity is needed for both anterior and posterior components. Overall, our results suggest that scaling is an intrinsic property of PAR proteins, which arises mainly from the combination of fixed protein concentrations and variations in surface/volume ratio.

Diffusion is the process most affected by temperature changes and exhibits an Arrhenius-type behavior

We next investigated how polarity establishment depends on temperature. Because temperature influences most molecular processes, all the parameters of the mathematical model could a priori depend on temperature. We thus considered that the three types of molecular mechanisms embedded in the model (i.e., protein diffusion, biochemical reactions, and cortical flows) might be affected differently by variations in temperature. To explore this possibility, we performed recordings at three temperatures spanning most of the viable range for *C. elegans* (13°C, 20°C, 24°C, Fig. 5, *A–C*) (18). Our analysis uncovered three changes with increased temperature: 1) a significant acceleration in the pace of polarity initiation (Fig. 5 *D*); 2) a loss of steepness in the gradient of the posterior domain during the maintenance phase (Fig. 5 *E*, *arrowheads*, (40)); and 3) a slight contraction of the relative length of the posterior domain (Fig. S10 *C*). To identify the source of these three modifications, we mimicked the impact of temperature on each group of related rates in the mathematical model using a scaling factor λ set to 1 at 20°C (see the Supporting Material).

We varied λs for the parameters representing protein diffusion (D_A and D_P), biochemical reactions (k_{A+}, k_{A-}, k_{AP}, k_{P+}, k_{P-}, and k_{PA}), or cortical flows (v) (Fig. S10, *D–R*, and Table S4). The exponents α and β were assumed to be unaffected by temperature, and the new flow measurements were used (M3). We found that varying the membrane binding rates (k_{A+}, k_{P+}, Fig. S10, *G–I*) reproduced both the contraction of relative domain length (Fig. S10 *I*) and the acceleration in polarity initiation (Fig. S10 *H*) but not gradient steepening (Fig. S10 *G*). Variations in cortical unbinding rates (k_{A-}, k_{P-}, Fig. S10, *J–L*) predicted only gradient steepening (Fig. S10 *J*), whereas variations in cortical flows reproduced only the acceleration in polarity initiation (v, Fig. S10, *P–R*). Moreover, variations in the mutual inhibition rates (k_{AP}, k_{PA}, Fig. S10, *M–O*) had almost no effect on the contraction of relative domain length (Fig. S10 *O*). By contrast, variations in diffusion could reproduce all three modifications (D_A, D_P, Figs. 5, *F* and *G*, and S10 *F*), suggesting that diffusion is the main process underlying the observed alterations in polarity establishment upon temperature changes.

To relate the scaling factors λ to the actual temperatures and to assess the contribution of parameters other than diffusion, we considered three increasingly complex mechanisms: 1) constant value for each temperature, e.g., in temperature-compensated cortical fluidity (41,42); 2) Arrhenius-type dependence for each temperature, e.g., in metabolic rates kinetics (43,44); and 3) independent values for each temperature, an arbitrary temperature dependence. These relations were hypothesized for the three types of molecular mechanisms encapsulated in the model. We then assessed the performance of different combinations of temperature mechanisms (Fig. S11 and the Supporting Material). The best model, selected using the Akaike information criterion with a correction or AICc (45), revealed again that diffusion is most sensitive to variations in temperature (Fig. S11 *A*). In addition, the selected model indicates that protein diffusion and biochemical reactions have Arrhenius-like kinetics (see the Supporting Material). Interestingly, in almost all models (Fig. S11, except Fig. S11 *D*), flows are independent of temperature, suggesting the existence of a compensation mechanism for cortical flows. We also conducted a parameter sensitivity analysis, which uncovered that polarity establishment is most robust to variations in diffusion parameters (Fig. S12, *E* and *I*). Such buffering of fluctuations in diffusion speeds indicates that significant variations in parameter value are required for a noticeable effect on polarization, hence providing an explanation for the identified strong dependence of diffusion on temperature.

Overall, we conclude that diffusion is more sensitive to variations in temperature than biochemical reactions, and that cortical flows appear to be largely constant within the studied temperature range.

DISCUSSION

We performed a quantitative analysis of polarity establishment in the early *C. elegans* embryo combining live imaging and mathematical modeling. To extend and further calibrate an extant mathematical model (M1 (13)), we first refined estimates of cortical flows, which are essential to account for the early dynamics of polarity establishment (M2, Fig. 6 *A*). Using an optimization method, we estimated previously unspecified parameters characterizing the mutual inhibition terms. Using our unique data on embryos of varying sizes, we derived a model that also accounts for part of the observed scaling of the PAR domains (M3, Fig. 6 *B*). Finally, we extended this model so that it also predicts temperature dependence of polarity establishment using Arrhenius-like equations (M4, Fig. 6, *C* and *D*). The lower magnitude of the variations predicted by the model following changes in size or temperature raises the possibility that some parameters did not converge to optimal values. However, the smoothness of the scoring function (Fig. S12) combined with the efficient convergence of the optimization (Fig. S7) render this hypothesis unlikely. Instead, we

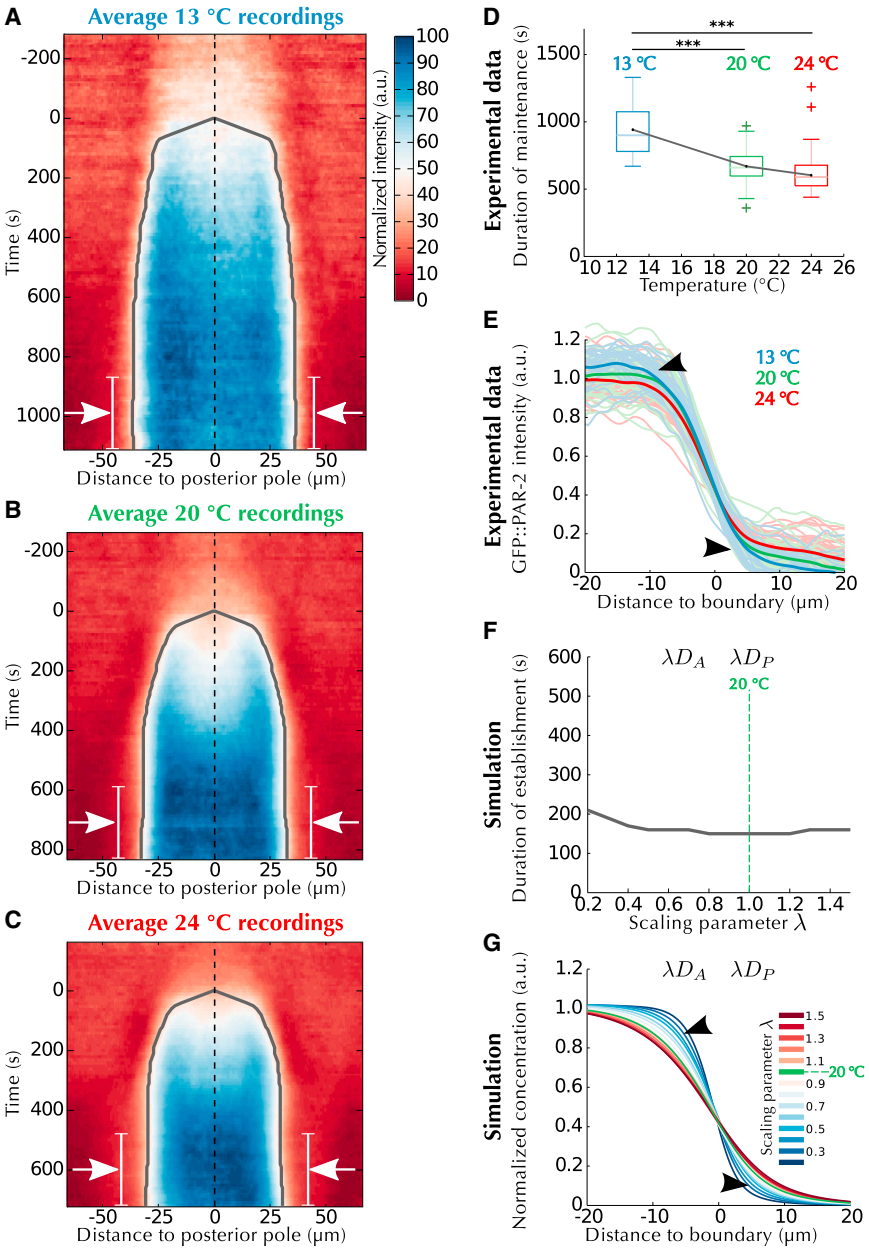

FIGURE 5 Diffusion is the process most affected by temperature. (*A–C*) Average kymographs of polarity establishment at the indicated temperatures, overlaid with landmarks similar to Fig. 1. Arrows: portion of the maintenance stage (*white line*) averaged for the profiles displayed in (*E*). (*D*) Quantification of duration of the maintenance phase (see the Supporting Material) at the three temperatures, overlaid with tests of significance (Student's two-tailed *t*-test). (*E*) Profiles of GFP::PAR-2 signal during maintenance (*arrows* in *A–C*) at different temperatures. Thin lines: individual profiles; thick lines: average of each condition. Each set of curves (i.e., each recording temperature) is statistically different from each other ($p < 0.001$, adaptive Neyman test (40)). Arrowheads: variations predicted by the model (see *G*). (*F*) Quantification of the time required for polarity maintenance as in (*D*) when the values of the diffusion parameters D_A and D_P are scaled by the factor λ. Note that the *x* axes in (*D*) and (*F*) cannot be directly compared; however, a similar trend is observed. (*G*) Profiles simulated by the model as in (*F*) and aligned as in (*E*). To see this figure in color, go online.

suggest that these remaining differences reflect simplifications inherent to mathematical modeling.

Indeed, the model from which our own analysis stems (13) did not consider certain aspects of polarity establishment. This includes the existence of other players of polarity establishment such as PAR-5 (46) or CDC-42 (47), potential feedback between polarity and cortical flows (8,35), and the individual dynamics of the different members of the anterior and posterior complexes. Nevertheless, we believe that the level of detail considered here is the most suitable mathematical representation of polarity establishment given the currently available experimental evidence. Of importance, such abstractions are important to reduce the number of parameters and permit their identifiability (Fig. S12). Moreover, despite its simplicity, model M1, and by extension its new variants M2–M4, can account for the behavior of various mutant/RNAi conditions that affect polarity establishment, including polarization in a no-flow regime or following changes in the ratio of anterior versus posterior proteins (13). A quantitative analysis in such embryos following the approach presented here should help further characterize the proposed mathematical model. In particular, studying polarity establishment upon depletion of proteins known to modulate the size of the domains, such as PAR-4 (48) or MEX-5/6 (8), would be highly informative.

Our work underscores the importance of cortical flows in the spatial and temporal dynamics of polarity establishment. Introducing newly determined flow values corrected

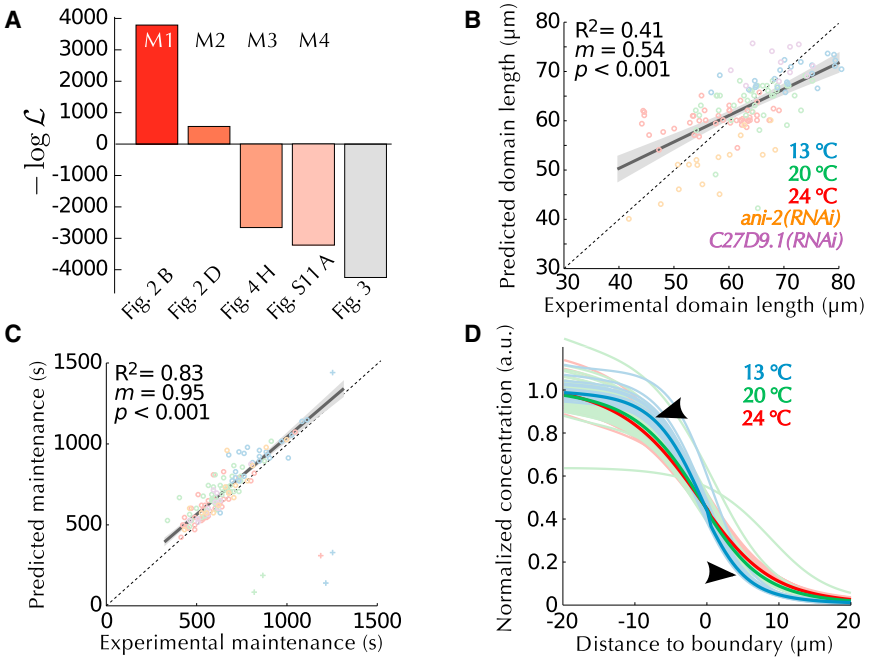

FIGURE 6 Predictions of the mathematical model obtained from size and temperature perturbations. (*A*) Performance (negative log-likelihood score) of the successive modifications of the mathematical model with an indication of the model used (*above*) and of the corresponding figure panel (*below*). The right-most gray bar corresponds to optimization of each embryo individually (Fig. 3) and is displayed for comparison. (*B*) Comparison between the experimental data and the predictions of the optimized model (M4) when the size of each embryo is used (*color-coded as indicated*). (*C*) Comparison between the experimental quantification of the duration of the maintenance phase and the predictions of M4. (*D*) Maintenance profiles simulated by the optimized model at different temperatures, to be compared with Fig. 5 *E*. To see this figure in color, go online.

spurious enrichment at the leading edge of the posterior domain (Fig. 2). Why was such an enrichment reported in embryos expressing GFP::PAR-2 in addition to endogenous PAR-2 (13)? Conceivably, PAR-2 levels could influence cortical flow velocity, through the anterior complex that can promote actomyosin contractility (9). In this scenario, higher PAR-2 levels may exclude anterior components more efficiently, hence increasing their concentration on the anterior. As for embryos expressing NMY-2::GFP (9), we suggest that higher levels of total NMY-2 cause increased cortical flows. Alternatively, it is conceivable that the manual tracking of NMY-2::GFP might have been biased toward selection of faster particles. Our analysis confirms that cortical mutual inhibition coupled to an overall fixed pool of proteins can explain the observed scaling and thus robustly pattern embryos of different sizes.

This model can also adapt to variations in temperature by incorporating an Arrhenius equation for the diffusion coefficient and the various reaction rates. The Arrhenius relation for diffusion relates to the viscosity of the medium (i.e., the cell cortex here, see the Supporting Material). Such an Arrhenius dependence is valid for an amorphous substance such as glass-like materials or colloidal gels (49) and has been observed in bacteria (50), indicating that biological material can exhibit such a type of viscous behavior. Whether the cortex of *C. elegans* displays similar features will be interesting to explore. Intriguingly, our results for cortical flows (Fig. S11) suggest relative insensitivity to variations in temperature, whereas cortical viscosity, which has been postulated to be an important factor in cortical flow dynamics (33), is predicted to be significantly affected by such variations. One potential explanation for this apparent conundrum is that variations in viscosity are balanced by changes in contractility throughout the probed temperature range.

Our approach combining a large data set with maximum-likelihood optimization allowed us to infer previously unspecified parameters governing mutual inhibition. Of importance, we found cooperativity of both anterior and posterior complexes to be required for polarity establishment. A previous model (14) proposed cooperativity between anterior proteins, in line with the evolutionarily conserved protein-protein interaction site in PAR-3 proteins that governs oligomerization (51). Here, we propose in addition that cooperativity is needed among posterior domain proteins. The underlying molecular tenets remain to be discovered, but may result from a different mechanism than in the anterior domain because no evidence of oligomerization has been reported among posterior components. One possibility is cooperative binding (37) between one or several of the posterior PAR proteins and the 14-3-3 protein PAR-5, which is necessary for efficient mutual inhibition (46). Alternatively, multisite phosphorylation of PAR-3 by PAR-1 (21) could provide such nonlinearity (38).

In conclusion, we performed a quantitative analysis of polarity establishment in *C. elegans* embryos that allowed us to identify hitherto undetermined parameters and refine a mathematical model to better account for variations in size and temperature. In addition and of importance, the automated pipeline that we developed provides an analytical framework adequate to investigate both the dynamics and the impact of other molecular players involved in polarity establishment.

SUPPORTING MATERIAL

Supporting Materials and Methods, twelve figures, four tables, and one movie are available at http://www.biophysj.org/biophysj/supplemental/S0006-3495(14)04769-9.

AUTHOR CONTRIBUTIONS

S.B., P.G., and F.N. designed the research; S.B. performed the experiments, with help from C.B.; S.B. implemented ASSET and the automated quantification procedures; S.B., P.G., and F.N. analyzed the data and wrote the manuscript.

ACKNOWLEDGMENTS

We are grateful to Fumio Motegi for the transgenic animals expressing GFP::PAR-2; *par-2(ok1723)*, as well as to Jonathan Bieler, Aude Blanchoud, Alessandro De Simone, Aitana Neves, and Virginie Hamel Hachet for useful comments on the manuscript. We also thank Nathan Goehring and Stephan Grill for insightful discussions on their model, as well as the MathWorks community and the Bio-Formats (52) for useful pieces of code.

This work was supported by grants from Josy Marty-Echec au Cancer de la Broye to S.B., from SystemsX.ch IPhD 51PH_0125979 to P.G. and F.N., as well as from the Swiss National Science Foundation to P.G. (3100A0-122500/1).

SUPPORTING CITATIONS

References (53–66) appear in the Supporting Material.

REFERENCES

1. Thompson, B. J. 2013. Cell polarity: models and mechanisms from yeast, worms and flies. *Development.* 140:13–21.
2. Martin-Belmonte, F., and M. Perez-Moreno. 2012. Epithelial cell polarity, stem cells and cancer. *Nat. Rev. Cancer.* 12:23–38.
3. Kemphues, K. J., J. R. Priess, …, N. S. Cheng. 1988. Identification of genes required for cytoplasmic localization in early *C. elegans* embryos. *Cell.* 52:311–320.
4. Gönczy, P. 2008. Mechanisms of asymmetric cell division: flies and worms pave the way. *Nat. Rev. Mol. Cell Biol.* 9:355–366.
5. Motegi, F., and A. Sugimoto. 2006. Sequential functioning of the ECT-2 RhoGEF, RHO-1 and CDC-42 establishes cell polarity in *Caenorhabditis elegans* embryos. *Nat. Cell Biol.* 8:978–985.
6. Schonegg, S., and A. A. Hyman. 2006. CDC-42 and RHO-1 coordinate acto-myosin contractility and PAR protein localization during polarity establishment in *C. elegans* embryos. *Development.* 133:3507–3516.
7. Jenkins, N., J. R. Saam, and S. E. Mango. 2006. CYK-4/GAP provides a localized cue to initiate anteroposterior polarity upon fertilization. *Science.* 313:1298–1301.
8. Cuenca, A. A., A. Schetter, …, G. Seydoux. 2003. Polarization of the *C. elegans* zygote proceeds via distinct establishment and maintenance phases. *Development.* 130:1255–1265.
9. Munro, E., J. Nance, and J. R. Priess. 2004. Cortical flows powered by asymmetrical contraction transport PAR proteins to establish and maintain anterior-posterior polarity in the early *C. elegans* embryo. *Dev. Cell.* 7:413–424.
10. Etemad-Moghadam, B., S. Guo, and K. J. Kemphues. 1995. Asymmetrically distributed PAR-3 protein contributes to cell polarity and spindle alignment in early *C. elegans* embryos. *Cell.* 83:743–752.
11. Boyd, L., S. Guo, …, K. J. Kemphues. 1996. PAR-2 is asymmetrically distributed and promotes association of P granules and PAR-1 with the cortex in *C. elegans* embryos. *Development.* 122:3075–3084.
12. Tostevin, F., and M. Howard. 2008. Modeling the establishment of PAR protein polarity in the one-cell *C. elegans* embryo. *Biophys. J.* 95:4512–4522.
13. Goehring, N. W., P. K. Trong, …, S. W. Grill. 2011. Polarization of PAR proteins by advective triggering of a pattern-forming system. *Science.* 334:1137–1141.
14. Dawes, A. T., and E. M. Munro. 2011. PAR-3 oligomerization may provide an actin-independent mechanism to maintain distinct par protein domains in the early *Caenorhabditis elegans* embryo. *Biophys. J.* 101:1412–1422.
15. Goehring, N. W., C. Hoege, …, A. A. Hyman. 2011. PAR proteins diffuse freely across the anterior-posterior boundary in polarized *C. elegans* embryos. *J. Cell Biol.* 193:583–594.
16. Maddox, A. S., B. Habermann, …, K. Oegema. 2005. Distinct roles for two *C. elegans* anillins in the gonad and early embryo. *Development.* 132:2837–2848.
17. Hara, Y., and A. Kimura. 2009. Cell-size-dependent spindle elongation in the *Caenorhabditis elegans* early embryo. *Curr. Biol.* 19:1549–1554.
18. Anderson, J. L., L. Albergotti, …, P. C. Phillips. 2011. Does thermoregulatory behavior maximize reproductive fitness of natural isolates of *Caenorhabditis elegans? BMC Evol. Biol.* 11:157.
19. Brenner, S. 1974. The genetics of *Caenorhabditis elegans*. *Genetics.* 77:71–94.
20. Kachur, T. M., A. Audhya, and D. B. Pilgrim. 2008. UNC-45 is required for NMY-2 contractile function in early embryonic polarity establishment and germline cellularization in *C. elegans*. *Dev. Biol.* 314:287–299.
21. Motegi, F., S. Zonies, …, G. Seydoux. 2011. Microtubules induce self-organization of polarized PAR domains in *Caenorhabditis elegans* zygotes. *Nat. Cell Biol.* 13:1361–1367.
22. Schonegg, S., A.-T. Constantinescu, …, A. A. Hyman. 2007. The Rho GTPase-activating proteins RGA-3 and RGA-4 are required to set the initial size of PAR domains in *Caenorhabditis elegans* one-cell embryos. *Proc. Natl. Acad. Sci. USA.* 104:14976–14981.
23. Grant, B., and D. Hirsh. 1999. Receptor-mediated endocytosis in the *Caenorhabditis elegans* oocyte. *Mol. Biol. Cell.* 10:4311–4326.
24. Kamath, R. S., A. G. Fraser, …, J. Ahringer. 2003. Systematic functional analysis of the *Caenorhabditis elegans* genome using RNAi. *Nature.* 421:231–237.
25. Kamath, R. S., M. Martinez-Campos, …, J. Ahringer. 2001. Effectiveness of specific RNA-mediated interference through ingested double-stranded RNA in *Caenorhabditis elegans*. *Genome Biol.* 2: RESEARCH0002.
26. Shelton, C. A., and B. Bowerman. 1996. Time-dependent responses to *glp-1*-mediated inductions in early *C. elegans* embryos. *Development.* 122:2043–2050.
27. Edelstein, A., N. Amodaj, …, N. Stuurman. 2010. Computer control of microscopes using μManager. *Curr. Protoc. Mol. Biol.* Chapter 14: Unit14.20.
28. Gorjánácz, M., I. W. Mattaj, and J. Rietdorf. 2007. Some like it hot. *Imaging Microsc.* 9:28–29.
29. Blanchoud, S., Y. Budirahardja, …, P. Gönczy. 2010. ASSET: a robust algorithm for the automated segmentation and standardization of early *Caenorhabditis elegans* embryos. *Dev. Dyn.* 239:3285–3296.
30. Goldstein, B., and S. N. Hird. 1996. Specification of the anteroposterior axis in *Caenorhabditis elegans*. *Development.* 122:1467–1474.
31. Rappleye, C. A., A. Tagawa, …, R. V. Aroian. 2002. The anaphase-promoting complex and separin are required for embryonic anterior-posterior axis formation. *Dev. Cell.* 2:195–206.
32. Niwayama, R., K. Shinohara, and A. Kimura. 2011. Hydrodynamic property of the cytoplasm is sufficient to mediate cytoplasmic streaming in the *Caenorhabditis elegans* embryo. *Proc. Natl. Acad. Sci. USA.* 108:11900–11905.

33. Mayer, M., M. Depken, …, S. W. Grill. 2010. Anisotropies in cortical tension reveal the physical basis of polarizing cortical flows. *Nature.* 467:617–621.
34. Hird, S. 1996. Cortical actin movements during the first cell cycle of the *Caenorhabditis elegans* embryo. *J. Cell Sci.* 109:525–533.
35. Cheeks, R. J., J. C. Canman, …, B. Goldstein. 2004. *C. elegans* PAR proteins function by mobilizing and stabilizing asymmetrically localized protein complexes. *Curr. Biol.* 14:851–862.
36. Bieler, J., C. Pozzorini, and F. Naef. 2011. Whole-embryo modeling of early segmentation in *Drosophila* identifies robust and fragile expression domains. *Biophys. J.* 101:287–296.
37. Colotti, G., A. Boffi, and E. Chiancone. 2008. Cooperativity and ligand-linked polymerisation in *Scapharca* tetrameric haemoglobin. *In* Dioxygen Binding and Sensing Proteins. M. Bolognesi, G. Prisco, and C. Verde, editors. Milano, Springer, Milan, pp. 107–119.
38. Gunawardena, J. 2005. Multisite protein phosphorylation makes a good threshold but can be a poor switch. *Proc. Natl. Acad. Sci. USA.* 102:14617–14622.
39. Sönnichsen, B., L. B. Koski, …, C. J. Echeverri. 2005. Full-genome RNAi profiling of early embryogenesis in *Caenorhabditis elegans*. *Nature.* 434:462–469.
40. Fan, J., and S. Lin. 1998. Test of significance when data are curves. *J. Am. Stat. Assoc.* 93:1007–1021.
41. Sinensky, M. 1974. Homeoviscous adaptation—a homeostatic process that regulates the viscosity of membrane lipids in *Escherichia coli*. *Proc. Natl. Acad. Sci. USA.* 71:522–525.
42. Hazel, J. R., and E. E. Williams. 1990. The role of alterations in membrane lipid composition in enabling physiological adaptation of organisms to their physical environment. *Prog. Lipid Res.* 29:167–227.
43. Gillooly, J. F., J. H. Brown, …, E. L. Charnov. 2001. Effects of size and temperature on metabolic rate. *Science.* 293:2248–2251.
44. Dell, A. I., S. Pawar, and V. M. Savage. 2011. Systematic variation in the temperature dependence of physiological and ecological traits. *Proc. Natl. Acad. Sci. USA.* 108:10591–10596.
45. Hurvich, C. M., and C.-L. Tsai. 1989. Regression and time series model selection in small samples. *Biometrika.* 76:297–307.
46. Morton, D. G., D. C. Shakes, …, K. J. Kemphues. 2002. The *Caenorhabditis elegans par-5* gene encodes a 14-3-3 protein required for cellular asymmetry in the early embryo. *Dev. Biol.* 241:47–58.
47. Gotta, M., M. C. Abraham, and J. Ahringer. 2001. CDC-42 controls early cell polarity and spindle orientation in *C. elegans*. *Curr. Biol.* 11:482–488.
48. Hung, T. J., and K. J. Kemphues. 1999. PAR-6 is a conserved PDZ domain-containing protein that colocalizes with PAR-3 in *Caenorhabditis elegans* embryos. *Development.* 126:127–135.
49. Doremus, R. H. 2002. Viscosity of silica. *J. Appl. Phys.* 92:7619–7629.
50. Parry, B. R., I. V. Surovtsev, …, C. Jacobs-Wagner. 2014. The bacterial cytoplasm has glass-like properties and is fluidized by metabolic activity. *Cell.* 156:183–194.
51. Li, B., H. Kim, …, K. Kemphues. 2010. Different domains of *C. elegans* PAR-3 are required at different times in development. *Dev. Biol.* 344:745–757.
52. Linkert, M., C. T. Rueden, …, J. R. Swedlow. 2010. Metadata matters: access to image data in the real world. *J. Cell Biol.* 189:777–782.
53. Abràmoff, M., P. Magalhães, and S. Ram. 2004. Image processing with ImageJ. *Biophotonics Int.* 11:36–42.
54. Amer, A., and E. Dubois. 2005. Fast and reliable structure-oriented video noise estimation. *IEEE Trans. Circ. Syst. Video Tech.* 15:113–118.
55. Bellman, R. 1952. On the theory of dynamic programming. *Proc. Natl. Acad. Sci. USA.* 38:716–719.
56. Olver, F. W. J., D. W. Lozier, R. F. Boisvert, and C. W. Clark. 2010. Chapter 19: Elliptic integrals. *In* NIST Handbook of Mathematical Functions. F. W. J. Olver, D. W. Lozier, R. F. Boisvert, and C. W. Clark, editors. Cambridge University Press, New York, NY, pp. 514–516.
57. Hansen, N., and A. Ostermeier. 2001. Completely derandomized self-adaptation in evolution strategies. *Evol. Comput.* 9:159–195.
58. Lagarias, J. C., J. A. Reeds, …, P. E. Wright. 1998. Convergence properties of the Nelder–Mead simplex method in low dimensions. *SIAM J. Optim.* 9:112–147.
59. Filzmoser, P., R. Maronna, and M. Werner. 2008. Outlier identification in high dimensions. *Comput. Stat. Data Anal.* 52:1694–1711.
60. Laidler, K. J. 1985. Chemical kinetics and the origins of physical chemistry. *Arch. Hist. Exact Sci.* 32:43–75.
61. Kawai, M., T. Kido, …, S. Ishiwata. 2006. Temperature change does not affect force between regulated actin filaments and heavy meromyosin in single-molecule experiments. *J. Physiol.* 574:877–887.
62. Jaqaman, K., D. Loerke, …, G. Danuser. 2008. Robust single-particle tracking in live-cell time-lapse sequences. *Nat. Methods.* 5:695–702.
63. Olivo-Marin, J.-C. 2002. Extraction of spots in biological images using multiscale products. *Pattern Recognit.* 35:1989–1996.
64. Smith, C. S., N. Joseph, …, K. A. Lidke. 2010. Fast, single-molecule localization that achieves theoretically minimum uncertainty. *Nat. Methods.* 7:373–375.
65. Hird, S. N., and J. G. White. 1993. Cortical and cytoplasmic flow polarity in early embryonic cells of *Caenorhabditis elegans*. *J. Cell Biol.* 121:1343–1355.
66. Tseng, Q., E. Duchemin-Pelletier, …, M. Théry. 2012. Spatial organization of the extracellular matrix regulates cell-cell junction positioning. *Proc. Natl. Acad. Sci. USA.* 109:1506–1511.

Biophysical Journal

Supporting Material

Quantitative Analysis and Modeling Probe Polarity Establishment in C. elegans Embryos

Simon Blanchoud, Coralie Busso, Félix Naef, and Pierre Gönczy

Supporting Material

Image analysis

PAR-2 levels were determined between late prophase (centration/rotation) and metaphase either on fixed specimen by immunofluorescence or on live embryos expressing GFP::PAR-2 (Fig. S1 E-F). Two regions of interest per embryo (posterior membrane *PM* and posterior background *PB*) were manually defined using a circular selection tool 9 pixels in diameter (Fig. S1 D) with the ImageJ software (1) and their pixel intensity analyzed with Matlab 2012b. Camera white noise and its standard deviation σ were automatically estimated (2) and averaged for each genotype. Posterior cortical signal was defined in a signal-to-noise ratio approach as $(PM - PB) / \sigma$ to compensate for the out-of-focus illumination visible in the posterior cytoplasm and normalized by setting the average of the wild-type measurements to 100% and the average of the *par-2(RNAi)* to 0%.

All recordings were automatically segmented and analyzed by ASSET (3) and the quantifications implemented either in Matlab 2012b or in C (all code used in this work is available upon request). To capture precisely the signal from the cortex, we developed a model of the image that consists of the background (both from the cytoplasm and the camera), the autofluorescence of the eggshell and the signal *per se* (Fig. S1 H-M). We approximated the cortical signal with a succession of 2D Gaussian functions $I = Ae^{-\frac{(x-\mu)^2}{2\sigma}}$, where A is the amplitude of the signal, μ the position of its center and σ its width. Spatial correlation between the values of the parameters of the model was imposed; in particular, we consider a constant thickness of the membrane by imposing σ to be constant throughout a recording. The background was taken as the smoothed projected image from which the cortex was deleted by replacing the portion between $\mu - 5\sigma$ and $\mu + 5\sigma$ with a linear interpolation of pixel intensity values at the border of this domain. The remaining parameters of the signal were then determined using a Levenberg-Marquardt optimization procedure developed by Manolis Lourakis. The autofluorescence of the eggshell is estimated from the GFP::PAR-2 channel on portions of the eggshell far enough from the cortex ($> 3\sigma$) using the same model as for the cortical signal, but constrained to a single set of parameters for each frame, and subtracted from

the cortical signal as a Gaussian function of the distance between the cortex and the eggshell. The different kymographs utilized to compute the temperature averages (Fig. 2 A and 5 A-C) were aligned such as to minimize their residuals.

We compensated for posteriorization, i.e. the process that re-centers the growing posterior domain to the closest pole (4, 5), by segmenting the center of the GFP::PAR-2 expression kymographs using dynamic programming (DP, 6), minimizing a cost function that mirrored the characteristics of the posterior domain. This function posited that the posterior domain is symmetric, relatively bright, centered at the posterior pole during maintenance and devoid of invaginations. Similarly, the position of the front of the posterior domain was determined using DP with a scoring function that favored pixels on the edge of a bright domain whose intensity value resembles the one observed during the maintenance phase. The parameters used in the different scoring functions were manually optimized through visual inspection and incorporated into a configuration file for ASSET. The duration of polarity maintenance was defined as the time between the moment the front of the domain, as identified by the automatic segmentation, has reached 77.5 % of its final length and the end of the recording (i.e. cytokinesis onset). This percentage was chosen as it corresponds to the portion of lowest variability (as defined by the mean of the squared residuals), taking steps of 2.5 %, when comparing the segmentation of the kymographs aligned for averaging. Note that this percentage also outperforms alignments based on the manual registration of cell cycle events (pronuclear meeting, pseudo-cleavage or cytokinesis onset).

Mathematical modeling and simulations

The model M1 (Eq. 2-3, 7) consists of a one-dimensional (assuming rotational symmetry along the longitudinal axis of the embryo) two-species (modeling the anterior and the posterior complexes at the plasma membrane) partial differential equation (as the model depends both on time and space). The model is composed of the following mathematical terms (Eq. 2):

(i) Rate of change in the concentration of the complexes at the plasma membrane.

(ii) Diffusion: the complex can freely diffuse when bound to the plasma membrane.

(iii) Mutual inhibition: one complex is excluded from the plasma membrane by the other complex. Each inhibition term contains a cooperativity factor (i.e. the exponents α and β) representing the degree of cooperative binding one complex exhibits when excluding the other complex from the membrane. Importantly, if either α or β is greater than one, the system can exhibit local bistability, which is necessary to achieve both a stable uniform unpolarized state at the onset of the process and a stable polarized state during the maintenance stage (7).

(iv) Binding: the complex binds from the cytoplasmic pool (Eq. 2) to the membrane.

(v) Unbinding: the complex detaches from the membrane to the cytoplasmic pool at a given rate.

(vi) Cortical flows: the complexes are displaced toward the anterior pole through an advection process. The resulting depletion of anterior complexes A near the posterior pole is the perturbation that permits the complex P to access the membrane to initiate polarity establishment. Note that cortical flows v vary over space and time.

This model assumes a constant total amount of proteins and a homogeneous cytoplasm; thus, the cytoplasmic pool is the difference between the membrane bound and the total amount of proteins (Eq. 3, 7), where ρ_A and ρ_P are the total amount of A and P respectively, L is the length of the cell membrane and φ is the surface to volume ratio relating the cortical and the cytoplasmic pools. φ is defined for a 3D ellipsoid with semiaxes $a \geq b \geq c$ as the ratio between the surface area S (Eq. 4, 8), where $F(\phi,k)$, $E(\phi,k)$ are incomplete elliptic integrals of the first and second kind respectively, $cos(\phi) = c/a$, and the ellipsoid volume is $V = \frac{3}{4}\pi abc$. Note that the semi-axis c is inferred from b using the result of a linear regression on the data extracted from differential interference contrast (DIC) 3D stacks of twenty embryos with a z resolution of 0.5 µm. The result of the regression is $c = 18.81 - 0.31b$ (R^2=0.99). The assumption that the cytoplasmic pool is well mixed is supported by the fast diffusion rates measured in the cytoplasm and the absence of cytoplasmic GFP gradient (9). Goehring and co-workers have experimentally determined the diffusion constants D_A and D_P, the on binding rates k_{A+} and k_{P+}, the off binding rates k_{A-} and k_{P-}, as well as the relative concentrations ρ_A and ρ_P (7, 9). We

utilized the geometric properties of each cell in the experimental dataset to define the surface to volume ratio φ as well as the membrane length L in the mathematical model in conjunction with the published parameter values (Table S1) and our flow measurements (Fig. 2 C).

All simulations of the model were performed using custom software developed in C, using finite-differences methods to solve the partial differential equations (PDE). For the spatial discretization, the diffusion is solved using a five-point central difference approximation, the advection using a second-order upwind scheme and the integral using the trapezoidal rule. Null derivative (Neumann) boundary condition was used for the protein concentration. The temporal discretization uses a Runge-Kutta-Fehlberg algorithm implemented by John Burkardt. While the time stepping is adaptive, simulations were carried out with 256 meshpoints, thus resulting in a spatial resolution of □0.25 μm, depending on the proportions of the simulated embryo. The initial concentrations used for the simulations were taken as the numerically identified value of the fixed point, in the absence of diffusion and advection, corresponding to the anterior complex being enriched at the membrane (7).

Model optimization

To quantitatively compare the results of the simulation of the mathematical model (Eq. 2-3, 7) with the data acquired in this work, the kymographs need to be synchronized to relate experimentally determined timing of one embryo with that of others, as well as to the timing of a simulation. To do so, we introduced for each embryo a shift factor δ_I for a given simulation S with respect to the experimental kymograph I, which is optimized together with the other parameters of the model. In addition, every kymograph is rescaled by setting the 0.1 % of the outer pixels, as defined by the segmentation of the posterior domain, to zero, and the 99.9 % of the inner pixels to one. Finally, to permit a meaningful comparison between the simulation and the experimental data, we adapted the spatial size of the simulation, L and φ, to match the dimensions of each embryo. We measure the length of the plasma membrane in the midplane of the embryo using the segmentation produced by ASSET to set L and we calibrate the surface to volume ratio of the embryo φ accordingly.

To quantify the resemblance between experiments and simulations, we defined the negative log-likelihood of a parameter set θ, given the set of experimental data Ω (Eq. 1), where I is a M_I by N_I pixels kymograph, S the corresponding simulated kymograph, D and B the positions of the domain boundary for I and S, respectively. The difference in pixel value (i.e. the right term) is rescaled by ε/N_I to have a weight comparable to that of the difference in boundary position (i.e. the left term) in the final score, given that typically $N_I \gg M_I$, where ε is a factor used to balance the influence of the pixel intensity with respect to the position of the boundary that was set to 0.25. In addition, a sigmoid function is applied to the boundary term to prevent the likelihood from being too sensitive to very minor changes in the segmentation of the posterior boundary. The boundary position term was added to the likelihood function to compensate for the lower sensitivity during the initiation stage (e.g. Fig. S2 E), which is due to a lower pixel intensity value at that time compared to the maintenance stage.

The optimization procedure was carried out in alternation by an evolution strategy with covariance matrix adaptation (CMA-ES, 10) and a Nelder-Mead simplex method (fminsearch, 11), both implemented in Matlab. Initial parameter values were generated by adding Gaussian noise first to the published values (7), then to the best values identified, finally to the average of the best value per embryo (Fig. 3). The best value among all these independent optimization runs was utilized in this work. In the optimization of the temperature adaptation models (Fig. S11), the four unmeasured parameters as well as the required shift factors δ_I were optimized together with the parameters of the various models.

Because our experimental setup does not provide information on the dynamics of the anterior domain, whereas the optimization procedure infers parameter values for this domain, we performed a set of 80 simulation experiments to assess the precision of such inferences (Fig. S7). In each experiment, a kymograph is simulated with the published values (7) for the four unmeasured parameters of the model (i.e. k_{AP}, α, k_{PA} and β), Gaussian white noise is added and the optimization procedure utilized to find back these values. Half of the optimization procedures were initialized at the correct values (k_{AP} = 0.19, α = 1, k_{PA} = 2 and β = 2), the other half further away from these values, at position where polarity could still be established (k_{AP} = 0.026, α = 1.97, k_{PA} = 0.014 and β = 2.42).

In addition, as described above, the shift factor δ_I was optimized as a fifth parameter, with the value of 0 being utilized for the simulated kymograph. Finally, different amounts of noise (10%, 25%, 50% and 100% of the parameter value) were added to the initial parameter value to study the convergence of the optimization procedure. With the exception of four optimizations that did not converge properly (i.e. that were detected as outliers based on their log-likelihood score using the algorithm detailed in the next paragraph), all 76 remaining simulation experiments converged properly towards the parameter value used in the simulation (Fig. S7). Importantly, the precision of the optimization procedure is maximal for the two cooperativity exponents α and β (Fig. S7 H, K).

To identify sets of parameters as outliers (i.e. $\{k_{AP}, \alpha, k_{PA}, \beta, \mathcal{L}\}$ in Fig. 3), we followed a principal component based approach that has been designed for multi-dimensional data (12). Given the amount of noise present in our data, we increased empirically the tolerance of this detection method, utilizing a larger c parameter by taking 25 times the median absolute deviation (MAD) of the distance, instead of 2.5, in the first biweight function (i.e. w_{1i}). We utilized the same algorithm for outliers identification in the convergence analysis (Fig. S7) but multiplying the MAD by 5.

Estimating cortical flows

To obtain a spatial and temporal map of the dynamics of cortical flows, we followed an indirect approach that utilizes the displacement of sub-cortical cytoplasmic yolk granules as a proxy for the movements of the contracting cortex. Importantly, while GFP::NMY-2 foci are best observed using cortical imaging (13), VIT-2::GFP permits midplane imaging, and thus the monitoring of movements both close to the male pronucleus during the early onset of flows as well as at the poles after posteriorization. Because measuring cortical flows obviously requires localizing the cortex, we inferred the position of the cell membrane in these frames (Fig. S4 A) using DP with a cost function based on VIT-2::GFP intensity. To infer the center of the forthcoming posterior domain, we detected the position of the male pronucleus by identifying the areas devoid of granules using two different intensity thresholds (Fig. S4 B), fitting the largest inscribed circle in each of these areas (Fig. S4 C) and tracking them over time until

pronuclear meeting using a custom implementation of a published algorithm (14). All the code utilized for measuring cortical flows was implemented using Matlab 2012b.

We detected the position of the fluorescent VIT-2::GFP granules (Fig. S4 D) by utilizing the "à trous" wavelet transform (Fig. S4 E, 19) to obtain an initial estimate, combined with an approach developed for super-resolution microscopy (16) to refine our detection (Fig. S4 F). A custom merging algorithm then discarded faint spots and computed the weighted average of overlapping particles (Fig. S4 G). The detected spots were then used as initial estimates for a second iteration of our detection pipeline (Fig. S4 H). The granules were then tracked using a custom implementation of an algorithm that performs this task by global optimization of the set of particle trajectories (Fig. S4 I, 18) without the gap closing, merging and splitting steps that were too computationally intensive for being implemented in this context. All the short tracks (< 5 frames) were then discarded; the directed speed of each remaining granule was then computed.

To determine the speed of the cortical flow at a particular location along the plasma membrane, we utilized a weighted average of the directed speeds using a spatial Gaussian kernel to favor exponentially more granules closest to the cortical actomyosin network. Such an approach should provide a more robust quantification than considering merely the closest granules. To quantify the precision of this approach, as well as to identify the most suitable kernel size, we carried out a set of simulation experiments using published velocity distributions of VIT-2::GFP granules (Fig. S5 A, (17)). We fitted cubic smoothing splines (csaps in Matlab) on the published values for the average posterior speed of the granules, as well as on the corresponding standard deviation, to infer a smooth speed distribution over the 14 µm range measured experimentally by those authors. This permits us to simulate sets of velocities for a given number of granules and with a distribution matching that of the experimental data, thus comparing the precision of different approaches for inferring the cortical speed (Fig. S5 B). We computed the error of the estimated cortical speed over 5000 realizations (i.e. the absolute difference with the true value), as well as its standard deviation, for a number of kernel sizes and particle number (Fig. S5 C, D). As anticipated, Gaussian weighting outperforms standard average for a wide range of kernel sizes, in particular for lower number of granules (Fig. S5 C). Interestingly, while larger kernels provide the less variable estimates (Fig. S5 D),

their inferred value is less precise on average because they take into account lower speeds further away from the cortex, hence underestimating the actual value at the cortex (Fig. S5 C). In the context of this trade-off between robustness and precision, we define the most adequate kernel size as the one minimizing the average error plus standard deviation between 10 and 450 granules (with a step size of 20 granules). Optimization was carried out using an evolution strategy with covariance matrix adaptation (CMA-ES, 10) and the best identified value found to be 0.895 µm (Fig. S5 E). Finally, to identify a potential bias in the inferred cortical speed, we computed the average estimated speed over the aforementioned range of granule number, and found it to be 92.8 % of the true value (Fig. S5 F). We thus compensate all cortical flow measurements for the 7.2 % underestimate inherent to a kernel of size 0.895 µm

A running average with a temporal window of 10 frames was applied to reduce the noise in the estimated velocities. The component of the velocity parallel to the segmentation of the cortex was kept (17). Finally, we compensated for posteriorization by performing this analysis relative to the position of the male pronucleus, which we tracked using the same algorithm (14). We quantified the cortical flows in recordings acquired in six embryos, tracking the movements of 1'729'820 particles in total, and aligned the embryos temporally to minimize the sum of flow map residuals. Note that because of the assumed rotational symmetry of polarity establishment, the two sides of the embryo were combined and thus flows are perfectly symmetric (Fig. 2 C). These 2D flows were utilized in all simulations except the original models (M1 and M1*), for which the original 2D flows were utilized (7). The flow values provided in Tables S1 and S2 were computed by averaging the pixels brighter than the mean plus two standard deviation of the respective 2D flow profiles.

In addition, we repeated this quantification by substituting the particle tracking step by particle image velocimetry (PIV, Fig. S6). PIV is a widespread flow quantification technique that has been used notably to quantify cortical flows in *C. elegans* (7, 17). Here, we utilized an ImageJ plugin to perform iterative PIV analysis (18). This comparison confirmed that the quantified flow profiles agreed between the two methods, both for individual recordings (Fig. S6 A-C), for the average flow profiles (Fig.

2 C and S6 D) and for the measured cortical speeds (Table S2), although a lower spatial resolution was obtained using PIV.

Cortical flows dependence on cell size

Assuming that the strength of the cortical flows depends on the fraction of bound myosin motors on actin filaments (19), it follows that these forces should depend on the inverse of the surface to volume ratio φ. For simplicity, we define the binding of myosin (M) on actin filaments (F) as a reversible three steps process (Eq. 5), where M_c and M_m are the fractions of cytoplasmic and membrane-bound myosin motors respectively, F_c and F_m the fraction of cytoplasmic and membrane-bound actin filaments and FM the force generating complex. We then write the law of mass action corresponding to the defined concentrations (Eq. 6) with symmetric equations for F_c and F_m. In addition, we hypothesize that the total pools of both myosin motors and actin filaments are fixed (Eq. 7), where M_T and F_T are the two total concentrations and φ is the surface to volume ratio. Moreover, because we want to determine the relation between FM and the proportions of the cell, we assume steady state for all the reactions. Finally, for simplicity, we approximate the cortical concentration of actin F_m as being constant (assuming the concentration of myosin motors is limiting, $k_B F_m = k_{BF}$); however, the relation between FM and φ computed without this hypothesis leads to the similar conclusion. Under these hypotheses, one can then compute the relation between FM and M_T.

Temperature dependence models

To adapt the model to variations in temperature, we considered three different equations for the diffusion constants (D^i, D^{ii}, D^{iii}), three for the biochemical reaction rates (k^i, k^{ii}, k^{iii}) and three for the flows (v^i, v^{ji}, v^{jii}). For all three mechanisms, the model i assumes a constant value for all the temperatures, thus being supposedly the worst model, and is used for comparison with more elaborate models. On the contrary, all models iii utilize independent values for each temperature. Note that, with the exception of k_{AP}, k_{PA} and v, which were not measured experimentally at 20 °C (9), all other parameters of the model have the published value (Tables S1, S2) imposed at 20 °C (i.e. all the temperature dependence models equal one at this temperature).

For the dependence to temperature of the reaction rates and flows, we utilized the Arrhenius equation $k_T = ke^{-\frac{E_k}{k_B T}}$, where k represents the so-called prefactor, E_k the activation energy of the reaction, T the absolute temperature in Kelvin and k_B the Boltzmann constant. This approach has been applied to a wide variety of biological processes, ranging from isolated biochemical reactions (20) to entire organisms (21). For the flows, we hypothesized that these are proportional to the fraction of active motors bound to actin filaments while the force of each motor remains constant (19), hence converting them to a motor binding reaction rate. For the adaptation of the diffusion coefficients to changes in temperature, we utilized the Stokes-Einstein equation $D_T = \frac{k_B T}{\zeta \eta_T}$, where η_T is the viscosity of the fluid and ζ the drag coefficient of the diffusing particle. Importantly, η_T itself depends on temperature through an unknown function. However, we approximate this relation using a thermally activated Arrhenius equation $\eta_T = \eta e^{\frac{E_D}{k_B T}}$, which is valid for colloidal gels (22).

Because the experimental measurements of the different reactions rates were performed at 20 °C on average (9), we set out to compute the conversion factors f_{kT} and f_{DT} that define the value of the different parameters at a temperature T such that $k_T = f_{k_T} k_{20}, D_T = f_{D_T} D_{20}$. We thus obtained two equations (Eq. 8-9) that depend only on the temperature T, their respective activation energy E_k and E_D as well as the Boltzmann constant k_B. In addition, we also optimized scaling parameters for k_{AP}, k_{PA} and ν because their value was not measured experimentally at 20 °C. All parameter values are provided in Table S4.

Equations

$$(1)\quad -\log \mathcal{L}(\theta \mid \Omega) = \sum_{I \in \Omega} \frac{M_I}{2} \log\left(\sum_{i=1}^{M_I} \frac{1}{1+e^{-(B_{i+\delta_I} - D_i)^2}} + \frac{\varepsilon}{N_I} \sum_{i=1}^{M_I} \sum_{j=1}^{N_I} \left(S_{i+\delta_I, j} - I_{i,j} \right)^2 \right)$$

$$\frac{\partial A}{\partial t} = D_A \frac{\partial^2 A}{\partial x^2} - k_{AP} A P^{\alpha} + k_{A_+} A_c - k_{A_-} A - \frac{\partial (\nu A)}{\partial x} \Bigg| \text{anterior complex}$$

(2)

$$\underbrace{\frac{\partial P}{\partial t}}_{\text{i}} = \underbrace{D_P \frac{\partial^2 P}{\partial x^2}}_{\text{ii}} - \underbrace{k_{PA} P A^{\beta}}_{\text{iii}} + \underbrace{k_{P_+} P_c}_{\text{iv}} - \underbrace{k_{P_-} P}_{\text{v}} - \underbrace{\frac{\partial (\nu P)}{\partial x}}_{\text{vi}} \Bigg| \text{posterior complex}$$

(3)

$$A_c = \rho_A - \frac{\varphi}{L} \int_{-\frac{L}{2}}^{\frac{L}{2}} A \mathrm{d}x$$

$$P_c = \rho_P - \frac{\varphi}{L} \int_{-\frac{L}{2}}^{\frac{L}{2}} P \mathrm{d}x$$

(4) $$S = 2\pi c^2 + \frac{2\pi ab}{\sin(\phi)} \left(E(\phi, k) \sin(\phi)^2 + F(\phi, k) \cos(\phi)^2 \right)$$

$$F_c \underset{k_{F-}}{\overset{k_{F+}}{\rightleftharpoons}} F_m$$

(5) $$M_c \underset{k_{M-}}{\overset{k_{M+}}{\rightleftharpoons}} M_m$$

$$F_m + M_m \underset{k_D}{\overset{k_B}{\rightleftharpoons}} FM$$

$$\frac{dM_c}{dt} = k_{M-} M_m - k_{M+} M_c$$

(6) $$\frac{dM_m}{dt} = k_{M+} M_c - k_{M-} M_m - k_B F_m M_m + k_D FM$$

$$\frac{dFM}{dt} = k_B F_m M_m - k_D FM$$

(7)

$$F_T = F_c + \varphi F_m + \varphi FM$$

$$M_T = M_c + \varphi M_m + \varphi FM$$

$$(8)\ f_{k_T} = \frac{k_T}{k_{20}} = \frac{ke^{-\frac{E_k}{k_B T}}}{ke^{-\frac{E_k}{k_B T_{20}}}} = e^{-\frac{E_k}{k_B}\left(\frac{1}{T}-\frac{1}{T_{20}}\right)}$$

$$(9)\ f_{D_T} = \frac{D_T}{D_{20}} = \frac{\frac{k_B T}{\zeta \eta_T}}{\frac{k_B T_{20}}{\zeta \eta_{20}}} = \frac{T}{T_{20}}\frac{\eta_{20}}{\eta_T} = \frac{T}{T_{20}} e^{-\frac{E_D}{k_B}\left(\frac{1}{T}-\frac{1}{T_{20}}\right)}$$

Supporting Tables

- **Table S1.** Published parameters of the model (Eq. 2-3). All the values are taken from published results (7, 9). Parameters determined empirically are highlighted with a gray background. v was computed by averaging the pixels brighter than the mean plus two standard deviation of the published 2D flow profile. φ and L were computed assuming a 54×30×30 µm embryo.

		Meaning	*Value*	*Std*	*Units*
Anterior domain	D_A	Diffusion coefficient	0.28	0.05	µm^2/s
	k_{AP}	Inhibition rate	0.19	-	µm^2/s
	α	Cooperativity exponent	1	-	-
	k_{A+}	Binding rate	0.00858	0.0017	µm/s
	k_{A-}	Unbinding rate	0.0054	0.005	1/s
	ρ_A	Total protein concentration	1.56	0.33	1/µm^3
Posterior domain	D_P	Diffusion coefficient	0.15	0.03	µm^2/s
	k_{PA}	Inhibition rate	2	-	µm^4/s
	β	Cooperativity exponent	2	-	-
	k_{P+}	Binding rate	0.0474	0.012	µm/s
	k_{P-}	Unbinding rate	0.0073	0.0057	1/s
	ρ_P	Total protein concentration	1	-	1/µm^3
	v	Cortical flows	0.1 [a)]	0.015 [a)]	µm/s
	φ	Surface to volume ratio	0.174	-	1/µm

L	Membrane length	134.6	-	µm

- **Table S2**. Published cortical flow speeds. Note that *N* corresponds to the number of particle tracked in the first two references, while it corresponds to the number of embryo analyzed in the other references. [a)] The value was computed by averaging the pixels brighter than the mean plus two standard deviation of the corresponding 2D flow profile. [b)] The value was computed by integrating the portion of the smoothed curve (as described in SM: Estimating cortical flows) above the mean plus one standard deviation of the corresponding 1D flow profile.

Reference	*Speed (µm/s)*	*N*	*Technique*
(23)	0.067 ± 0.013	17	Manual tracking of microinjected fluorescein-phalloidin aggregates
(24)	0.067 ± 0.008	≥48	Slope of DIC granules kymograph
This work	0.071 ± 0.008 [a)]	6	VIT-2::GFP particle tracking
This work	0.075 ± 0.011 [a)]	6	VIT-2::GFP particle image velocimetry
(17)	0.080 ± 0.007 [b)]	6	VIT-2::GFP particle image velocimetry
(25)	0.090 ± 0.007 [b)]	75	NMY-2::GFP particle image velocimetry
(7)	0.11 ± 0.015 [a)]	4	NMY-2::GFP particle image velocimetry
(13)	0.128 ± 0.017	6	Slope of NMY-2::GFP kymograph

- **Table S3.** Calibrated values for the unmeasured parameters. The two first models utilize the published empirical values (7). Note that lower values for the mutual inhibition rates (k_{AP} and k_{PA}) are required to account for the low GFP::PAR-2 signal on the anterior half of the embryo (Fig. S2). Units are as in Table 1.

	k_{AP}	α	k_{PA}	β
M1 (7)	0.19	1	2	2
M1* (optimized values)	0.001	4.81	0.075	3.15
M2 (new flows)	0.19	1	2	2
Average of all best values	0.043 ± 0.12	1.97 ± 1.26	0.34 ± 1.39	2.14 ± 0.78

Average without outliers	0.008 ± 0.017	2.17 ± 1.28	0.030 ± 0.035	2.30 ± 0.74
M3 (size calibrated)	0.002	2.09	0.014	2.36
M4 (temperature model)	0.002 ± 0.001	2.09 ± 0.16	0.014 ± 0.001	2.36 ± 0.09

- **Table S4**. Parameters of the various temperature models (Fig. S11, see Materials and Methods). Note that for the models *iii*, the two values correspond to the direct impact of temperature on the rates at 13 °C and 24 °C respectively (i.e. instead of an activation energy as written in the header). Note also that v represents the scaling applied to the cortical flows (Fig. 2 C) at 20 °C. Units are as in Table S1.

Fig. S11	*Model*	k_{AP}	k_{PA}	v	E_D	E_k	E_v
A	D^{ii}, k^{ii}, v^{j}	0.0027	0.0144	0.81	0.85	0.32	0
B	D^{i}, k^{i}, v^{j}	0.0028	0.0146	0.79	0	0	0
C	D^{ii}, k^{ii}, v^{ji}	0.0025	0.0136	0.87	0.88	0.36	0.0001
D	$D^{iii}, k^{iii}, v^{iii}$	0.0025	0.0138	0.87	1.34;1.69	1.02;1.20	1.08;0.75
E	D^{i}, k^{ii}, v^{j}	0.0025	0.0135	0.79	0	0.0001	0
F	D^{i}, k^{i}, v^{ji}	0.0026	0.0140	0.78	0	0	0.0007
G	D^{i}, k^{ii}, v^{ji}	0.0025	0.0136	0.76	0	0.0014	0.0014
H	D^{ii}, k^{i}, v^{j}	0.0025	0.0137	0.90	0.32	0	0
I	D^{iii}, k^{i}, v^{j}	0.0026	0.0142	0.84	0.85;1.36	0	0
J	D^{iii}, k^{ii}, v^{ji}	0.0025	0.0136	0.75	0.48;1.53	0.36	0.0003
M4	D^{ii}, k^{ii}, v^{j}	0.0023	0.0132	0.86	0.80	0.23	0

Supporting Movie

- **Movie S1**. Representative triple channel time-lapse recording of a wild type GFP::PAR-2; *par-2(ok1723)*; mCherry::PH embryo. The recorded channels are (top) DIC, (middle) mCherry::PH, (bottom) GFP::PAR-2; the raw data is displayed in each case. This recording corresponds to the frames used in Fig. 1 and S1 and has been accelerated 60 times. See also Fig. S1D.

Supporting Figures

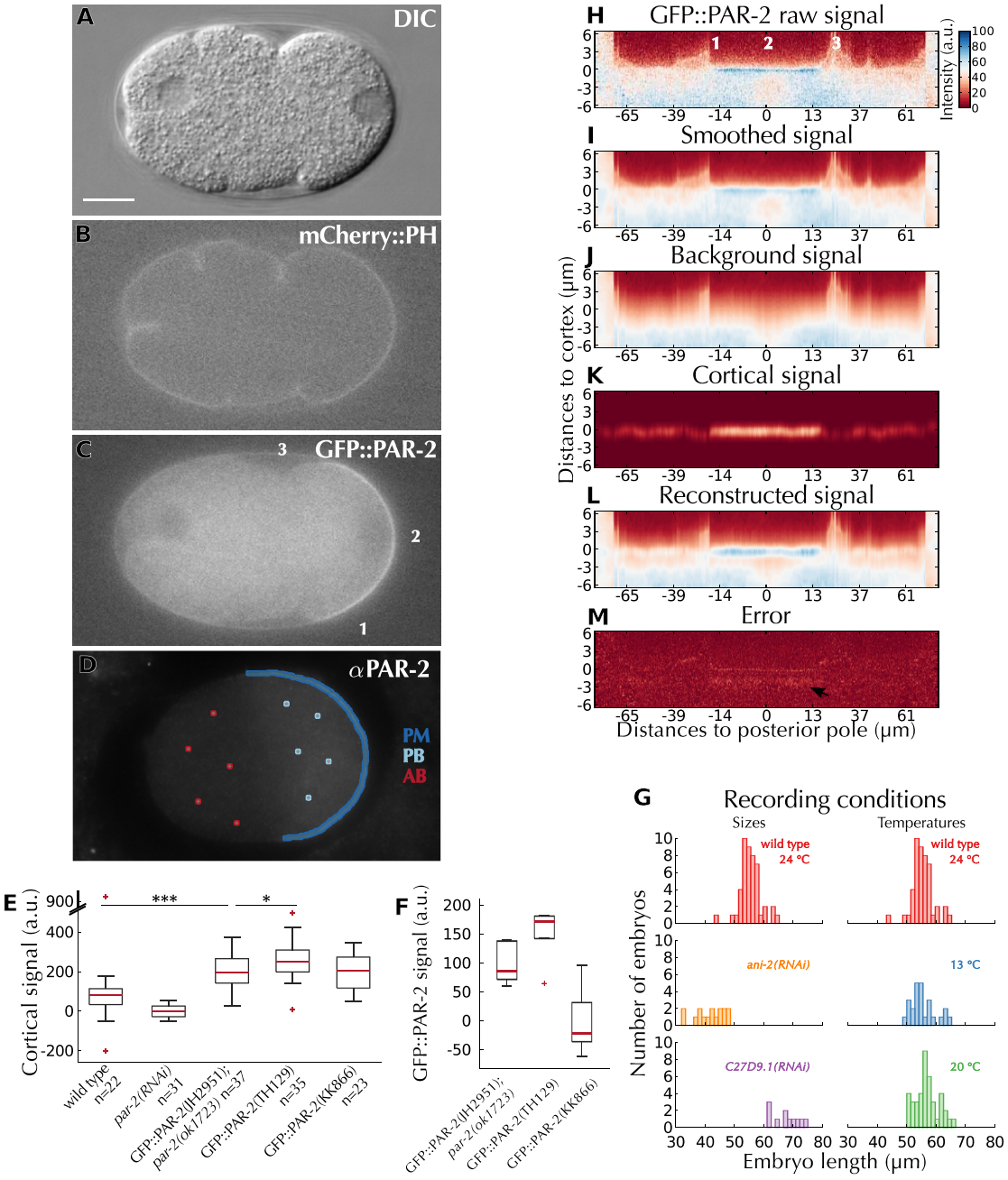

- **Figure S1**. Monitoring polarity establishment. (**A-C**) Frame from representative triple channel time-lapse recording (**A** DIC, **B** mCherry::PH, **C** GFP::PAR-2). Numbers in **C** and **H** denote corresponding locations. Scale bar: 10 µm. (**D**) Sample immunofluorescence image from the strain used in this study, overlaid with the two manually defined regions of interest (color-coded) utilized for signal quantification (see

Supporting Material). *AB* represents what we considered as the anterior background, by opposition to the quantified posterior background (*PB*). (**E**) Comparison of PAR-2 protein levels in strains of indicated genotype. The means of the RNAi and of the wild type are defined as 0% and 100%, respectively. The strain used in this study is JH2951, the one used by Goehring *et al.* TH129. For each boxplot, the horizontal red line represents the median, the box ranges from the 25th to the 75th percentile and the whiskers extend to the entire distribution of data points with the exception of outliers depicted by red crosses. Note that in all figures, statistical significance (here using a Student's two-tailed *t*-test) is indicated by: * $p < 0.05$, ** $p < 0.01$, *** $p < 0.001$. (**F**) Comparison of the expression level of the GFP::PAR-2 transgene in strains of indicated genotype. *n=5* for every genotype. (**G**) Distribution of embryo lengths in different recording conditions: *ani-2(RNAi)* (*n=16*), *C27D9.1(RNAi)* (*n=11*), 24 °C (*n=47*), 13 °C (*n=25*), 20 °C (*n=41*). The 24 °C is represented twice for comparison with both datasets. (**H**) Raw perpendicular quantification of the image in **C** based on the segmentation performed by ASSET. (**I**) Perpendicular quantification of image in **C** smoothed using a Gaussian filter. The background signal (**J**) is separated from the cortical signal (**K**) as described in the Supporting Material. (**L**) Signal reconstructed using the described quantification procedure. (**M**) Difference between **H** and **L** indicate that only little information is lost below the posterior domain (arrow).

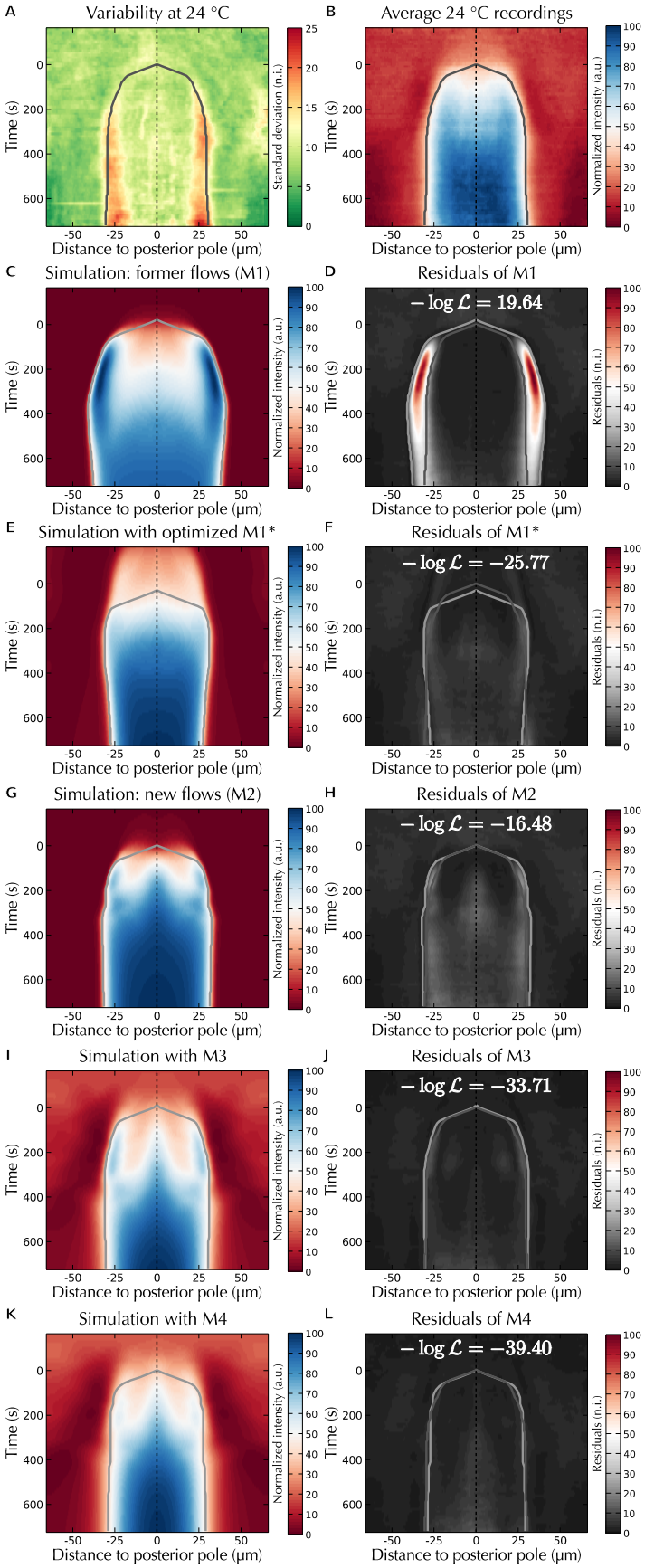
A
Variability at 24 °C
B
Average 24 °C recordings
C
Simulation: former flows (M1)
D
Residuals of M1
$-\log \mathcal{L} = 19.64$
E
Simulation with optimized M1*
F
Residuals of M1*
$-\log \mathcal{L} = -25.77$
G
Simulation: new flows (M2)
H
Residuals of M2
$-\log \mathcal{L} = -16.48$
I
Simulation with M3
J
Residuals of M3
$-\log \mathcal{L} = -33.71$
K
Simulation with M4
L
Residuals of M4
$-\log \mathcal{L} = -39.40$
Time (s)
Distance to posterior pole (µm)
Standard deviation (n.i.)
Normalized intensity (a.u.)
Residuals (n.i.)

- **Figure S2**. Prediction of the model with new cortical flow measurements is quantitatively improved with respect to experimental data. (**A**) Standard deviation of the average corresponding to **B** (n.i.: normalized intensity, i.e. the same scale as **B**). Note that the highest variation is located along the boundary of the domain towards the end of polarity maintenance. (**B**) Average protein expression during polarity establishment at 24 °C, overlaid with segmentation of the center of the domain (dashed black line) and of the domain expansion (dark gray). (**C**) Simulation of the mathematical model from Goehring *et al.* (Eq. 2-3) using the published parameter values and cortical flows (Table S1). The kymograph is overlaid with the segmentation of the domain (light gray). (**D**) Residuals between the experimental data in **B** and the simulation in **C**, overlaid with both segmentations and the negative log-likelihood score. (**E**) Same as in **C** but using optimized parameter values. (**F**) Residuals between the simulation in **B** and the experimental data in **E**, overlaid with both segmentations, using the same color map as **D**. (**G-H**) Same as in **C-D** but as predicted using the flows quantified using VIT-2::GFP particle tracking. The absence of leading edge enrichment is reflected in the reduction of the log-likelihood. (**I-J**) Same as in **C-D** but as predicted using model M3 (i.e. after calibration with the median kymographs). (**K-L**) Same as in **C-D** but for model M4 (i.e. implementing in addition the most likely temperature dependence model calibrated on the median kymographs, Fig. 6).

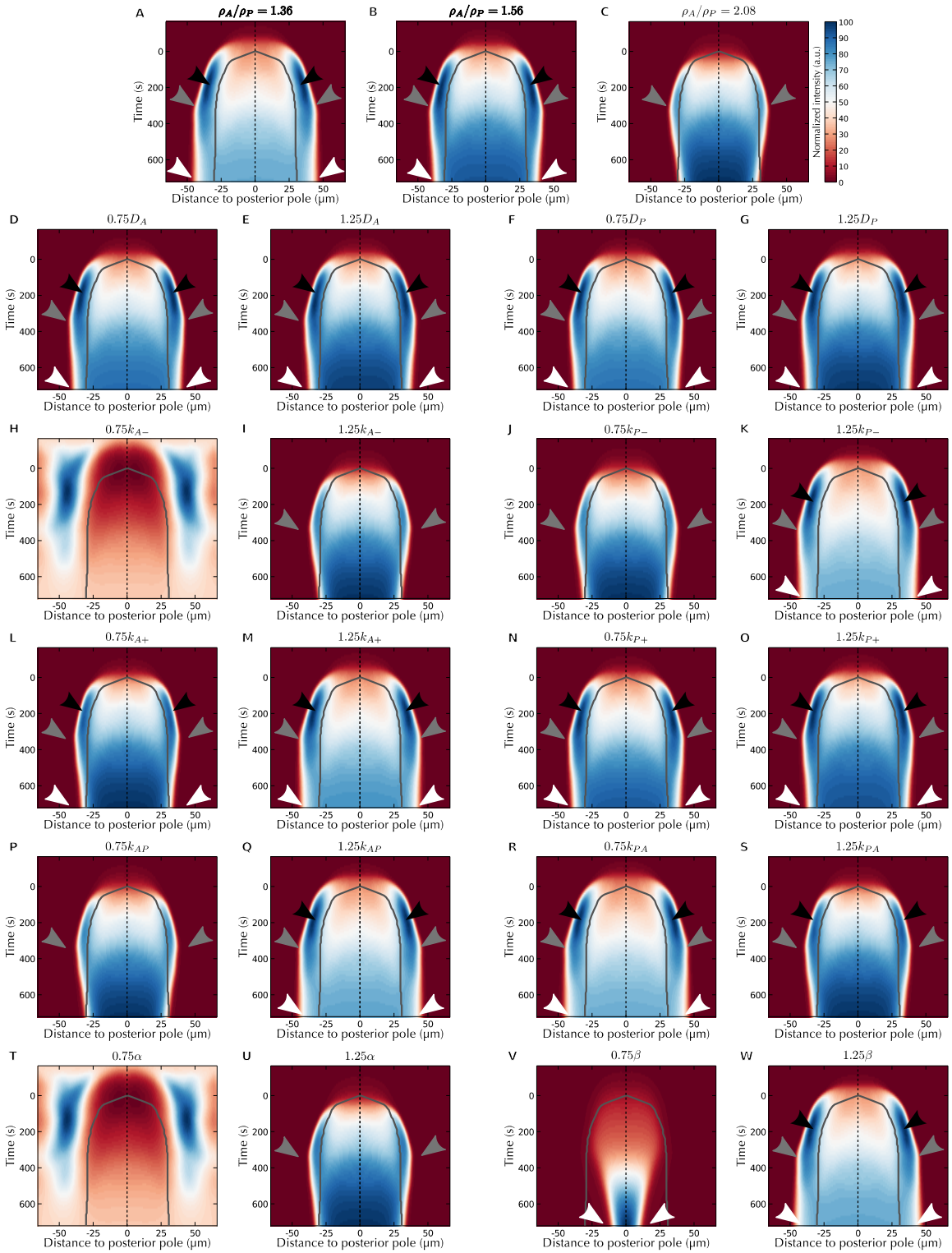

- **Figure S3**. Varying published parameter values does not attenuate leading edge enrichment. (**A-C**) Varying the relative level of posterior proteins. Simulation of the mathematical model from (7) using the published parameter values and cortical flows

(M1) with the indicated relative level of posterior proteins (above). The kymograph is overlaid with the segmentation of the experimental domain at 24 °C (dark gray) and the center of the domain (dashed black line). The relative concentration of the anterior versus posterior proteins (ρ_A/ρ_P) has been measured experimentally, using the ratio between the fluorescence expression of GFP::PAR-6 and GFP::PAR-2, to be 1.56 (i.e. **B**, (7)). Black arrowheads indicate the salient leading front enrichment not observed experimentally (see Fig. 2 A), gray arrowheads the concomitant domain overshooting and white arrowheads point at the extent of the posterior domain. (**D-E**) Same as **A** and **C** but varying the anterior diffusion coefficient D_A. Note that the reference kymograph for this variation is still **B**. (**F-G**) Same as **D-E** but varying the posterior diffusion coefficient D_P. (**H-K**) Same as **D-G** but varying the binding rates k_{A+} and k_{P+}. (**L-O**) Varying the unbinding rates k_{A-} and k_{P-}. (**P-S**) Varying the mutual inhibition rates k_{AP} and k_{PA}. (**T-W**) Varying the cooperativity coefficients α and β. Note that in **H** and **T**, polarity is not established because of the high uniform level of the posterior proteins throughout the simulation. Note also that none of these variations corrects both the enrichment and the overshooting.

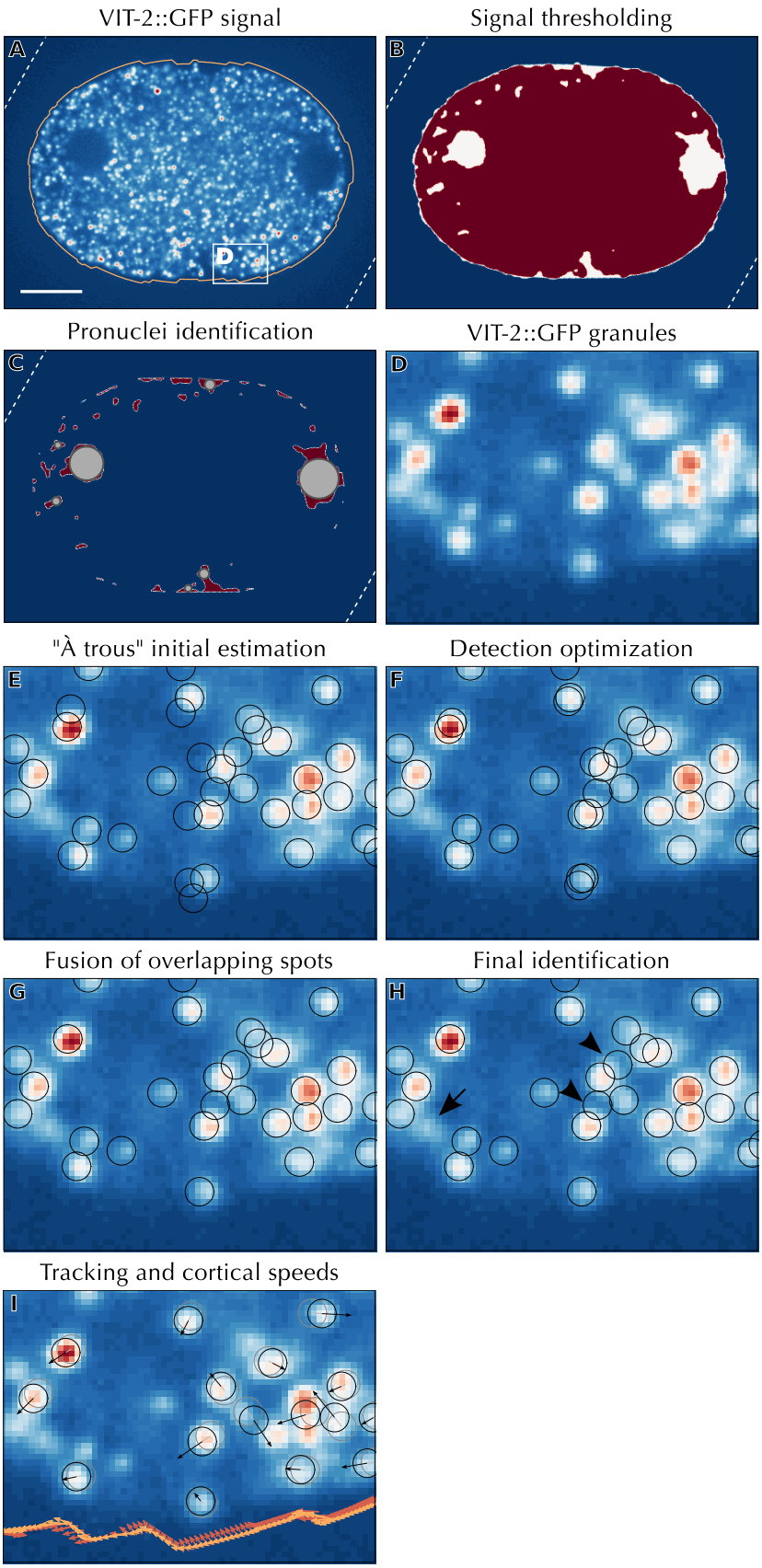
VIT-2::GFP signal
Signal thresholding
A
B
D
Pronuclei identification
VIT-2::GFP granules
C
D
"À trous" initial estimation
Detection optimization
E
F
Fusion of overlapping spots
Final identification
G
H
Tracking and cortical speeds
I

- **Figure S4**. Detection and tracking of VIT-2::GFP granules. (**A**) Raw GFP image utilized to detect the yolk granules overlaid with the segmented cortex (orange). The scale bar represents 10 µm and the white box delimits the area magnified in panels **D-I**. The white dashed lines in **A-C** delimit the boundary of the raw image. (**B**) Segmentation of the GFP image using two different intensity thresholds. The lower one delimits the entire embryo (white) while the higher one retains the area in which granules can be located (red). (**C**) Identification of candidate positions for the pronuclei. The areas devoid of granules (red) are overlaid with the largest inscribed circles (gray) representing candidate pronuclei. (**D**) Magnification of the area delimited in **A**. (**E**) Localization using the "à trous" wavelet transform. (**F**) Result of the spot detection optimization procedure (see Supporting Material). (**G**) Fusion of the overlapping detections in **F**. (**H**) Final estimation after a second round of optimization and fusion. The arrow indicates a missed granule, the arrowheads detection mistakes, typically discarded by the tracking algorithm (see Supporting Material). (**I**) Tracking of the detected yolk granules (black circle) linked with their position in the previous frame (gray circle) and the resulting displacement (black arrow). The averaged displacement (red) and the component parallel to the cell cortex (i.e. cortical flow, orange) are depicted on the cell membrane.

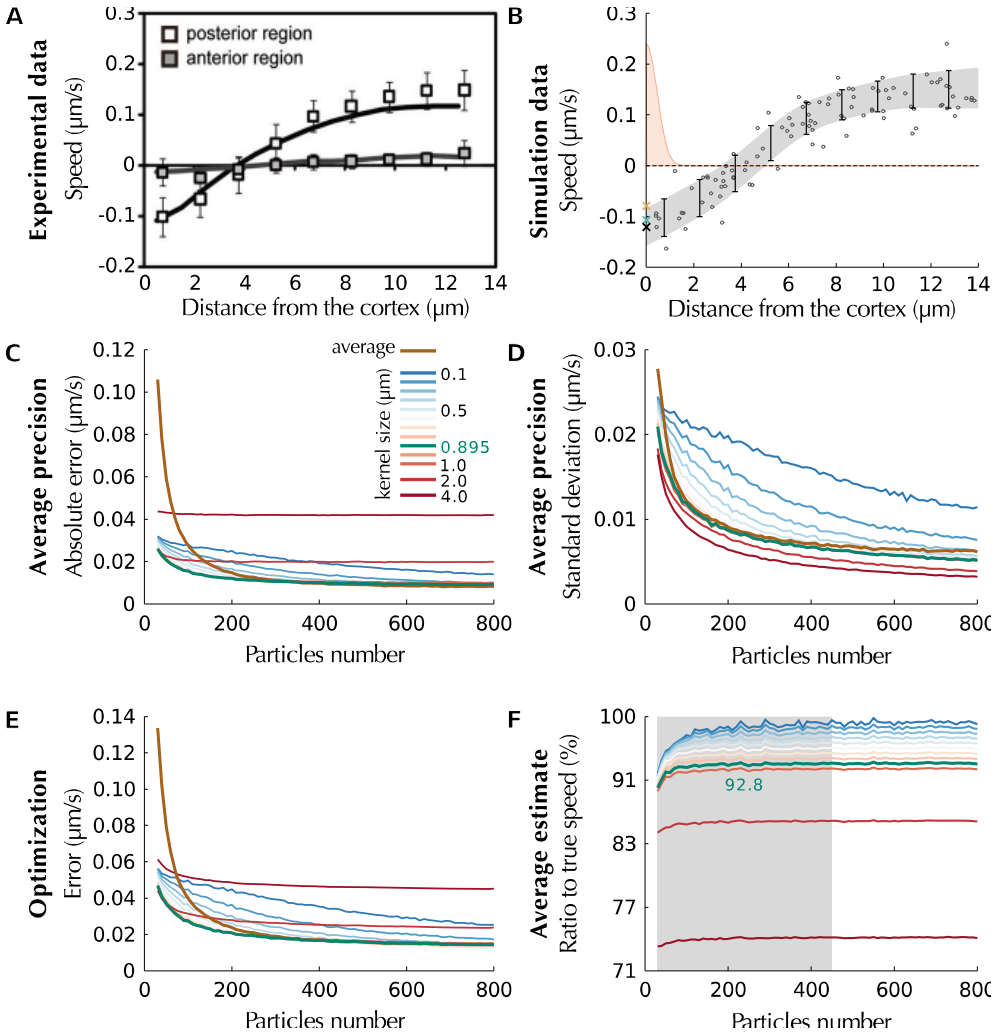

- **Figure S5.** Precision of cortical flow measurements using particle tracking. (**A**) Published *in vivo* speed distribution of VIT-2::GFP granules (from 17). (**B**) Simulation experiment of 100 granule speeds following the distribution in **A** (black circles). Overlaid are the averages and standard deviations extracted from **A** (black), their polynomial interpolation (gray), the extrapolated cortical speed (black cross), the weight distribution for the optimal Gaussian kernel size of 0.895 µm (pink, see SM), the corresponding cortical speed estimation (turquoise cross) and the estimation obtained by averaging the 15 closest granules from the cortex (brown cross). (**C**) Comparison of the average precision of the estimated cortical flow for a wide range of granule number and kernel sizes, color-coded as indicated. (**D**) Standard deviation of the corresponding estimates in **C**, color-coded as in **B**. (**E**) Error function used by the optimization algorithm to identify

the most adequate kernel size (average plus standard deviation), color-coded as in **B**. (**F**) Average estimated cortical speed for the kernel sizes color-coded as in **B**. Overlaid in gray is the range of granule numbers, the average of which was used to compensate the underestimation resulting from a kernel size of 0.895 µm.

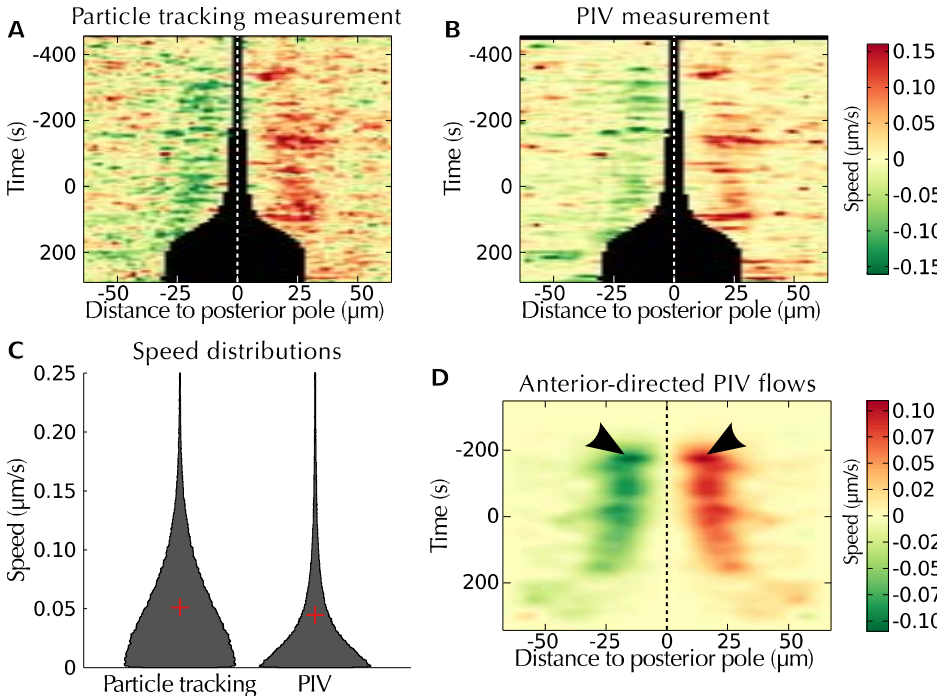

- **Figure S6.** Cortical flow quantification using particle image velocimetry (PIV). (**A**) The cortical flow profile of a single VIT-2::GFP recording using the particle tracking approach (see Fig. S4 and S5). The black area in the center of the flow profile corresponds to the portion of the cortex masked by the male pronucleus. (**B**) The cortical flow profile of the same recording as in **A** but using PIV instead of particle tracking. The color code is identical between **A** and **B**. Note that except for the lower resolution obtained in **B**, the two profiles appear almost identical. (**C**) Comparison of the distribution of speed magnitudes between the particle tracking approach and PIV. All six flow profiles were pooled for these violin plots where the normalized histogram of speed magnitudes is depicted in black and the corresponding mean value as a red cross. Note that mean value for PIV (0.045 µm/s) is slightly lower than for particle tracking (0.051 µm/s). Note also that a long tail in both distributions was cut at 0.25 µm/s. (**D**) The average 2D flow profile obtained using PIV. Note that, except for a stronger initial pulse (arrowheads), the PIV approach leads to similar results than the presented particle tracking method (compare with Fig. 2 C).

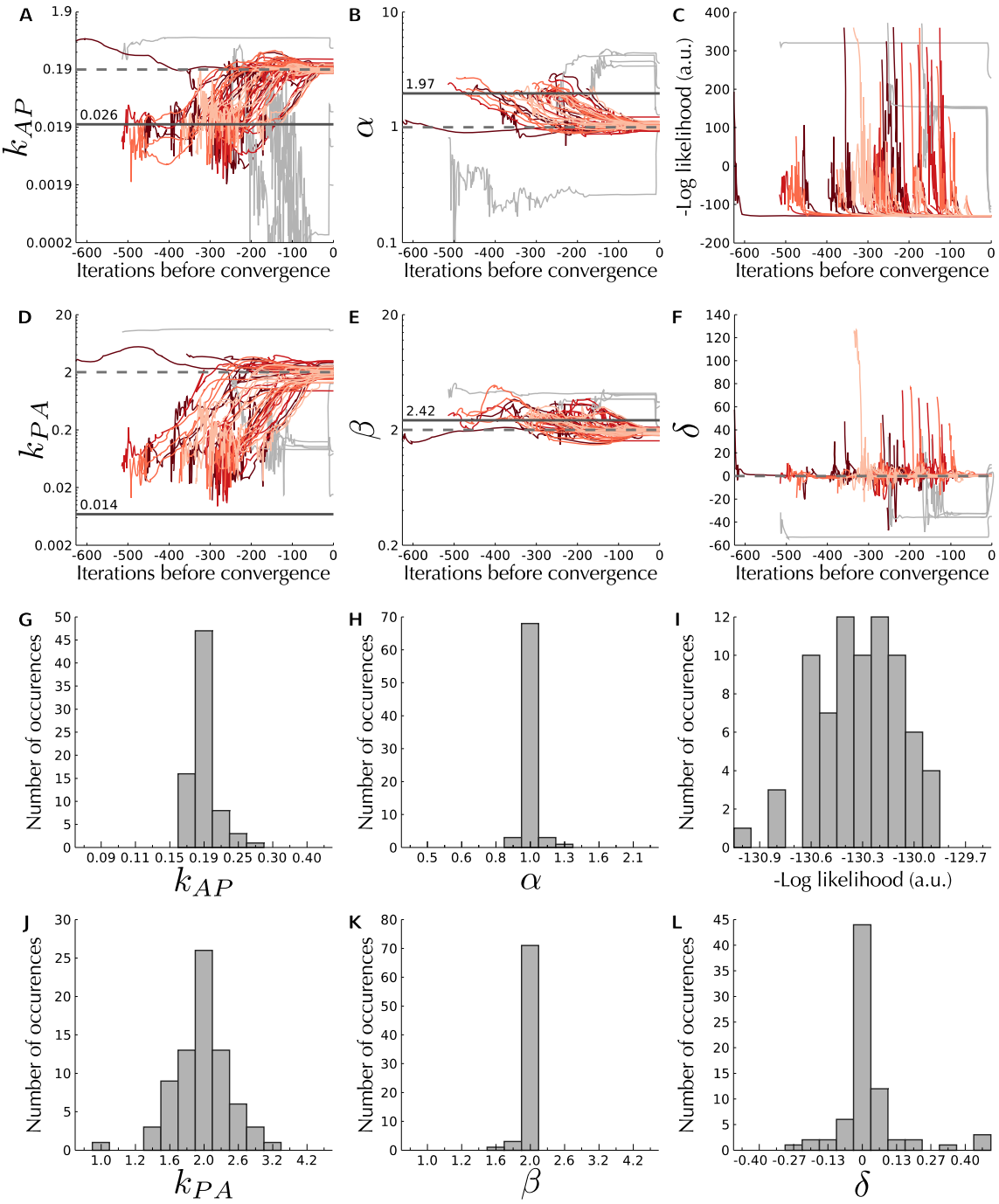

- **Figure S7**. The maximum-likelihood optimization procedure converges in simulation experiments. (**A-F**) Time traces for the optimization procedure of the indicated model parameters in 80 simulations experiments. Half of the optimization procedures were initialized around the correct values (depicted by the dashed gray line) while the other half were initialized around the values represented by the solid black line, with the corresponding value inscribed above it. Different shades of red indicate different amounts

of noise (10%-lightest, 25%, 50% and 100%-darkest) added to the initial value of the parameters while the gray lines indicate the four optimizations that did not converge properly (i.e. that were detected as being outliers based on their log-likelihood score). Note that no shift was introduced in the reference kymographs, hence the optimal value for the shift factor δ (see SM) is 0. (**G-L**) Distribution of the identified most-likely parameter value after convergence. All four unmeasured parameters, as well as the shift factor δ (see SM), are correctly identified by the optimization procedure. Note that the cooperativity exponents α and β are more tightly defined than the two inhibition rates k_{AP} and k_{PA}. Note also that these simulation experiments were performed using uncompensated cortical flows (i.e. 92.8 % of the actual speeds, see SM: Estimating cortical flows). However, because the convergence of these simulation experiments depends on the smoothness of the parameter space rather than on the cortical flow value, using such reduced speeds does not affect these results.

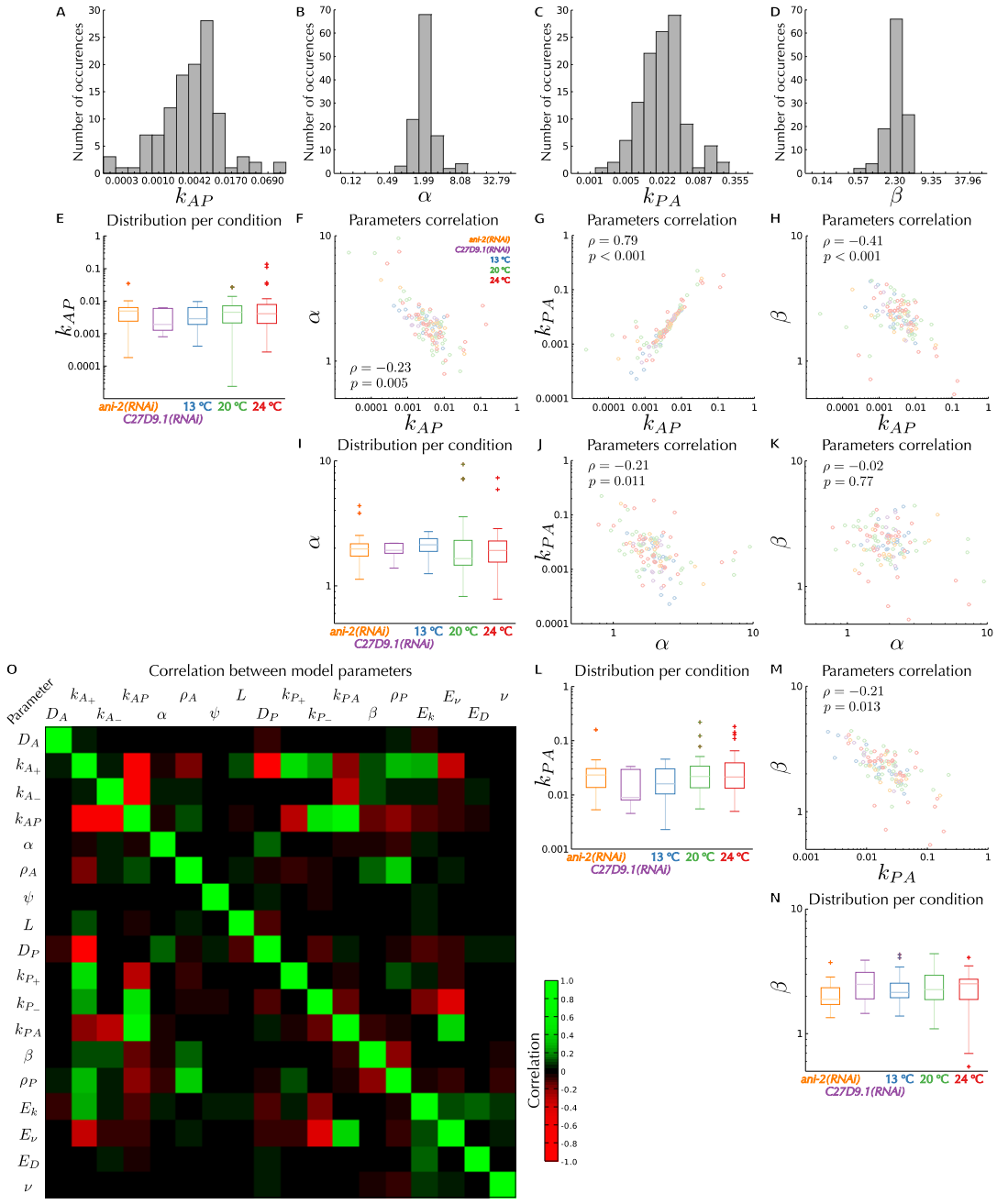

- **Figure S8**. Distribution of the most likely parameters for each embryo. (**A-D**) Distribution of the best value for the unmeasured inhibition parameters identified for each embryo independently. (**E**) Distribution of the inhibition rate k_{AP} per condition, color-coded as indicated. Statistical significance between all five different recording conditions was tested using Student's two-tailed *t*-test. Correlation between k_{AP} and (**F**) the anterior cooperativity exponent α, indicated is the corresponding Pearson's correlation coefficient ρ and the corresponding *p*-value (Student's t-distribution for a transformation of the

correlation), (**G**) the posterior inhibition term k_{PA} and (**H**) the posterior cooperativity term β respectively. (**I**) Distribution per condition of α. Correlation between α and (**J**) k_{PA} and (**K**) β respectively. (**L**) Distribution per condition of k_{PA} and (**M**) its correlation with β. (**N**) Distribution per condition of β. Note the high positive correlation between k_{AP} and k_{PA}, indicating that the value of these two parameters needs to be carefully balanced for polarity to establish properly. Note also the lower correlation observed between the inhibition rates k_{AP} and k_{PA}, and the cooperativity exponents α and β. This implies that a potential underestimation of the inhibition rates would lead to a reduction of the cooperativity exponents. Consequently, maximum care was taken in quantifying the signal on the anterior domain (see SM: Image Analysis) to ensure that k_{AP} or k_{PA} bear their proper values. Note also that, as in the simulation experiments (Fig. S7), the cooperativity exponents α and β are more tightly defined than the two inhibition rates k_{AP} and k_{PA} (compare **B** and **D** with **A** and **C**). (**O**) Correlation matrix for model M4. Each entry in the matrix represents the correlation, as indicated by the color code, between the corresponding column/row pair of parameters of the model. Positive correlation (green) highlights parameters whose joint variation has a minor influence on the likelihood score. On the contrary, negative correlation (red) points at parameters whose mutual compensation influences little the likelihood score. By contrast, black indicates parameters that cannot compensate for each other. The matrix was computed using a numerical approximation of the Hessian matrix (26).

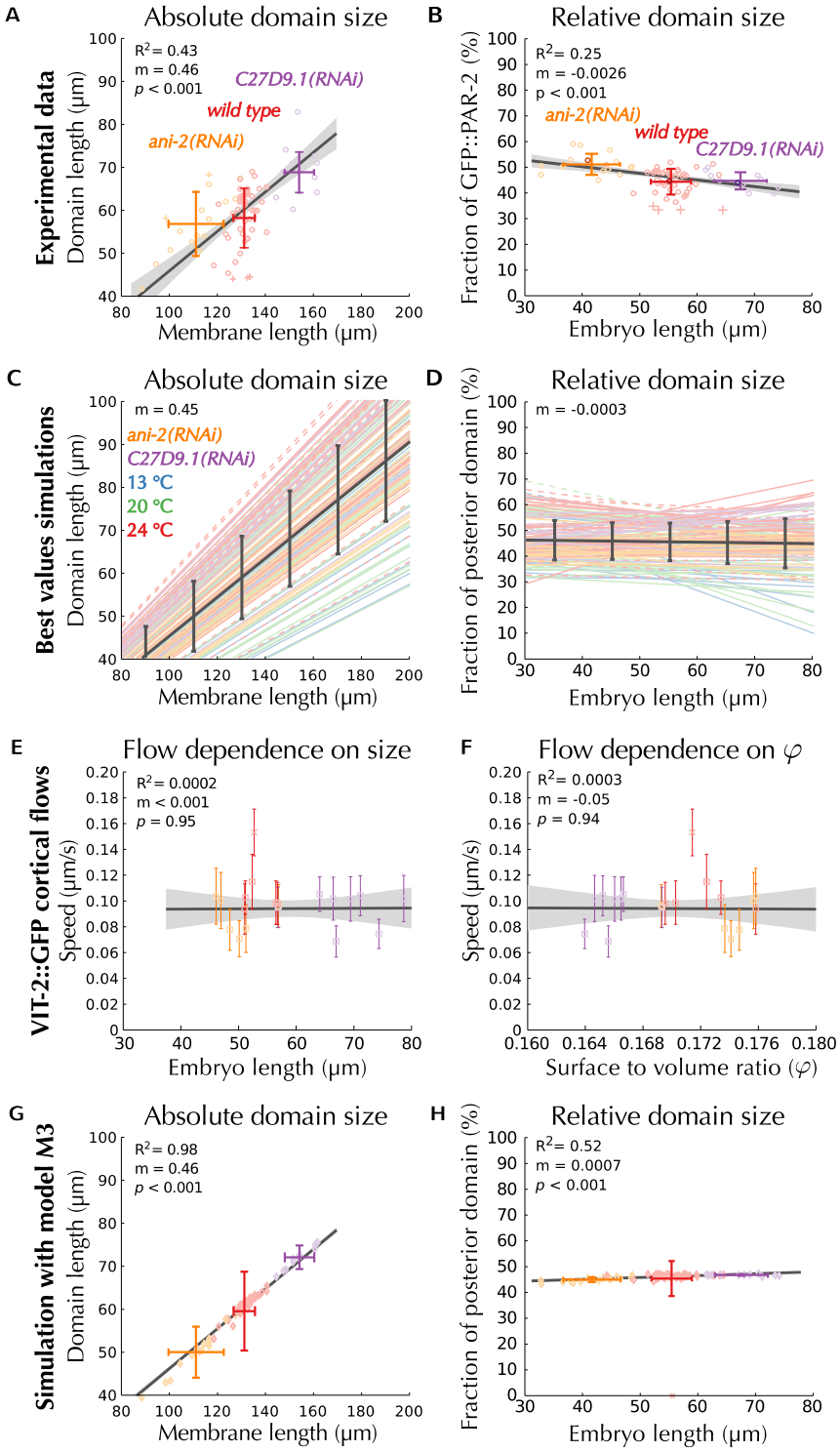

- **Figure S9**. Adaptations of the posterior domain size to variations in embryo size. (**A**) Correlation between membrane length and the length of the posterior domain in embryos from the color-coded recording condition, overlaid with the linear regression (dark gray line), the 95% confidence interval for the estimated regression coefficients (light gray

area), the correlation coefficient R^2, the slope of the correlation m and the p-value (Student's two-tailed t-test for the coefficient m). Note that in this representation of the data, the slope m corresponds to the average length of the posterior domain. (**B**) Correlation between embryo size and the relative fraction of membrane occupied by the posterior domain as observed experimentally, overlaid with the same information as in **A**. The darker circles indicate the location of the median recordings depicted in Fig. 4. Note that **A** and **B** are redundant. However, the imprecision in the domain scaling is more apparent in **B** while **A** is a more intuitive representation of the scaling process. (**C**) Correlation between membrane length and the length of the posterior domain as predicted when the most likely set of parameter values $\{k_{AP}, \alpha, k_{PA}, \beta\}$ of each embryo (see Fig. 3) is utilized. Thin lines represent the linear regression (similar to the thick black line in **A**) obtained from the domain length predicted by a set of parameter value, color-coded as the recording condition the corresponding embryo belongs to (i.e. similar to Fig. 3). Dashed lines correspond to the regression from parameter values identified as outliers in Fig. 3. Overlaid are the average of the regression slopes (black line), the corresponding standard deviation (whiskers) and the slope of the average correlation m. (**D**) Same as C but between embryo size and the relative fraction of membrane occupied by the posterior domain. (**E**) Absence of correlation between embryo length and cortical flow speed. The color code is the same as in **A**. Note that velocities are slightly higher than in Table S2 because here we display the average of the absolute speeds. (**F**) Same as in **E** but between the surface to volume ratio of the embryo and cortical flow speed. (**G**-**H**) Same as in **A** and **B** but as predicted by model M3 (i.e. using the values calibrated with the median recordings). Note also that panels **B** and **H** are the same as Fig. 4 G and H and are depicted here for comparison with **D**.

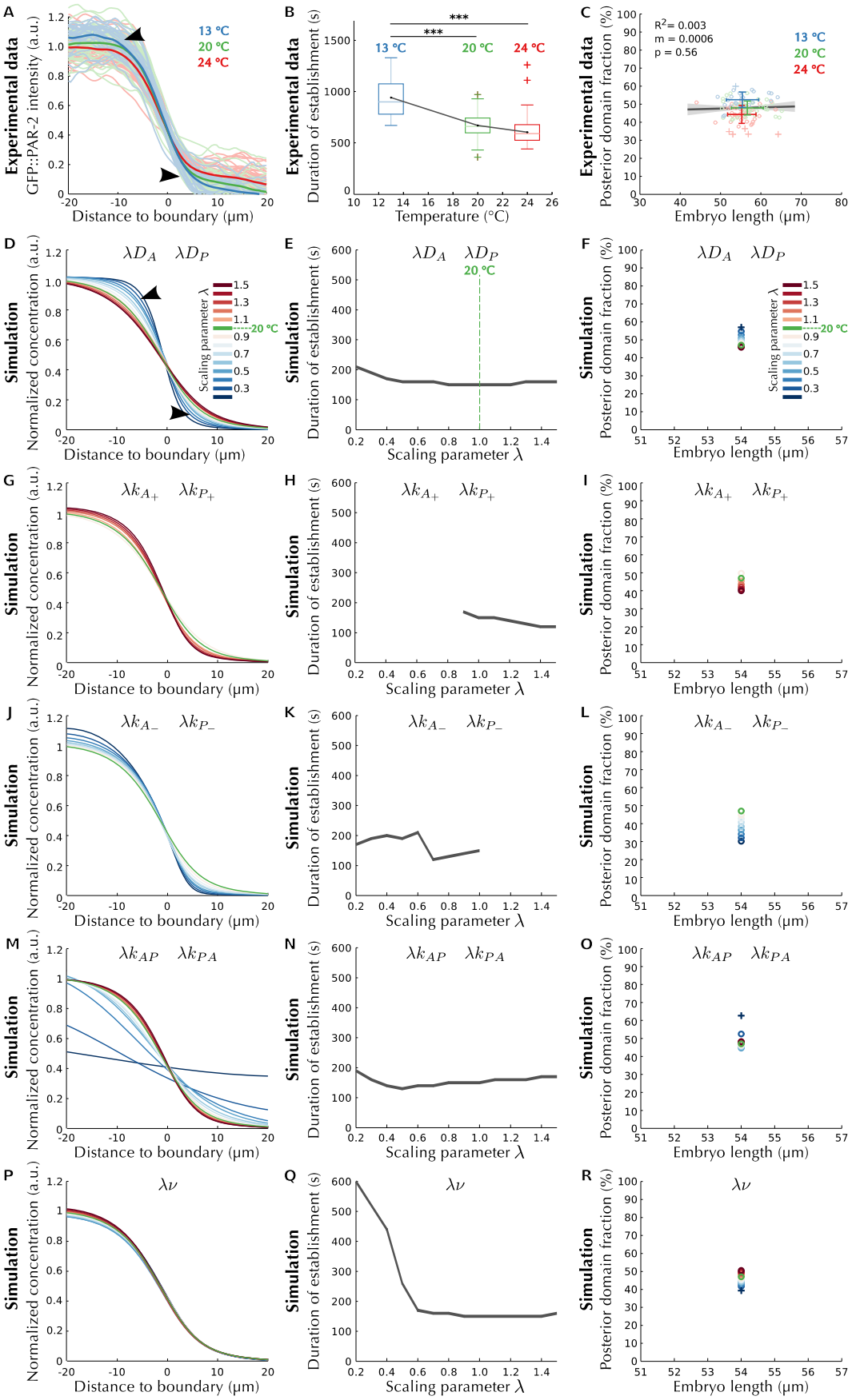
A
Experimental data
GFP::PAR-2 intensity (a.u.)
13 °C
20 °C
24 °C
Distance to boundary (μm)
B
Experimental data
Duration of establishment (s)
***
***
13 °C
20 °C
24 °C
Temperature (°C)
C
Experimental data
Posterior domain fraction (%)
R²= 0.003
m = 0.0006
p = 0.56
13 °C
20 °C
24 °C
Embryo length (μm)
D
Simulation
Normalized concentration (a.u.)
λD_A λD_P
Scaling parameter λ
1.5
1.3
1.1
20 °C
0.9
0.7
0.5
0.3
Distance to boundary (μm)
E
Simulation
Duration of establishment (s)
λD_A λD_P
20 °C
Scaling parameter λ
F
Simulation
Posterior domain fraction (%)
λD_A λD_P
Scaling parameter λ
20 °C
Embryo length (μm)
G
Simulation
Normalized concentration (a.u.)
λk_A+ λk_P+
Distance to boundary (μm)
H
Simulation
Duration of establishment (s)
λk_A+ λk_P+
Scaling parameter λ
I
Simulation
Posterior domain fraction (%)
λk_A+ λk_P+
Embryo length (μm)
J
Simulation
Normalized concentration (a.u.)
λk_A− λk_P−
Distance to boundary (μm)
K
Simulation
Duration of establishment (s)
λk_A− λk_P−
Scaling parameter λ
L
Simulation
Posterior domain fraction (%)
λk_A− λk_P−
Embryo length (μm)
M
Simulation
Normalized concentration (a.u.)
λk_AP λk_PA
Distance to boundary (μm)
N
Simulation
Duration of establishment (s)
λk_AP λk_PA
Scaling parameter λ
O
Simulation
Posterior domain fraction (%)
λk_AP λk_PA
Embryo length (μm)
P
Simulation
Normalized concentration (a.u.)
λν
Distance to boundary (μm)
Q
Simulation
Duration of establishment (s)
λν
Scaling parameter λ
R
Simulation
Posterior domain fraction (%)
λν
Embryo length (μm)

- **Figure S10**. Diffusion is the only process in the model whose variation reproduces the trends observed *in vivo* upon variation of the recording temperature. (**A-C**) Monitoring polarity establishment at three different temperatures (color-coded) exhibits (**A**) a flattening of the domain gradient, (**B**) an increase in the pace of polarization and (**C**) a slight contraction in the relative length of the posterior domain. (**D-F**) Variations in the diffusion coefficients (D_A and D_P jointly) by the nondimensional scaling parameter λ to mimic the impact of temperature in the absence of a temperature dependence model. Upon increasing values of λ (i.e. at increasing temperatures), the model predicts all three trends observed *in vivo*: (**D**) a flattening of the domain gradient (arrowheads), (**E**) an increase in the pace of polarization and (**F**) a slight contraction in the relative length of the posterior domain. Note that because of the absence of a temperature dependence model, the relation between the value of λ and temperature is unknown and thus the y-axis in **D**, the x-axis in **E** and the y-axis in **F** are not directly comparable to those in **A-C**. (**G-I**) Changes in profile, timing and relative domain size when the on rates (k_{A+} and k_{P+}) are varied. (**J-R**) Similar to **D-F** but when the off rates (k_{A-} and k_{P-}), the mutual inhibition rates (k_{AP} and k_{PA}) or the flow speeds (v) are varied, respectively. Note that no other parameter besides the diffusion coefficients (**D-F**) recapitulates all three trends observed experimentally (**A-C**). Note also that some of these rates could potentially be reduced upon increasing temperature. However, no parameter exhibits an inversion in all three trends with increasing λ. In addition, note that panels **A**, **B**, **D** and **E** are the same as Fig. 5 D-G and H and are depicted here for comparison with the other panels.

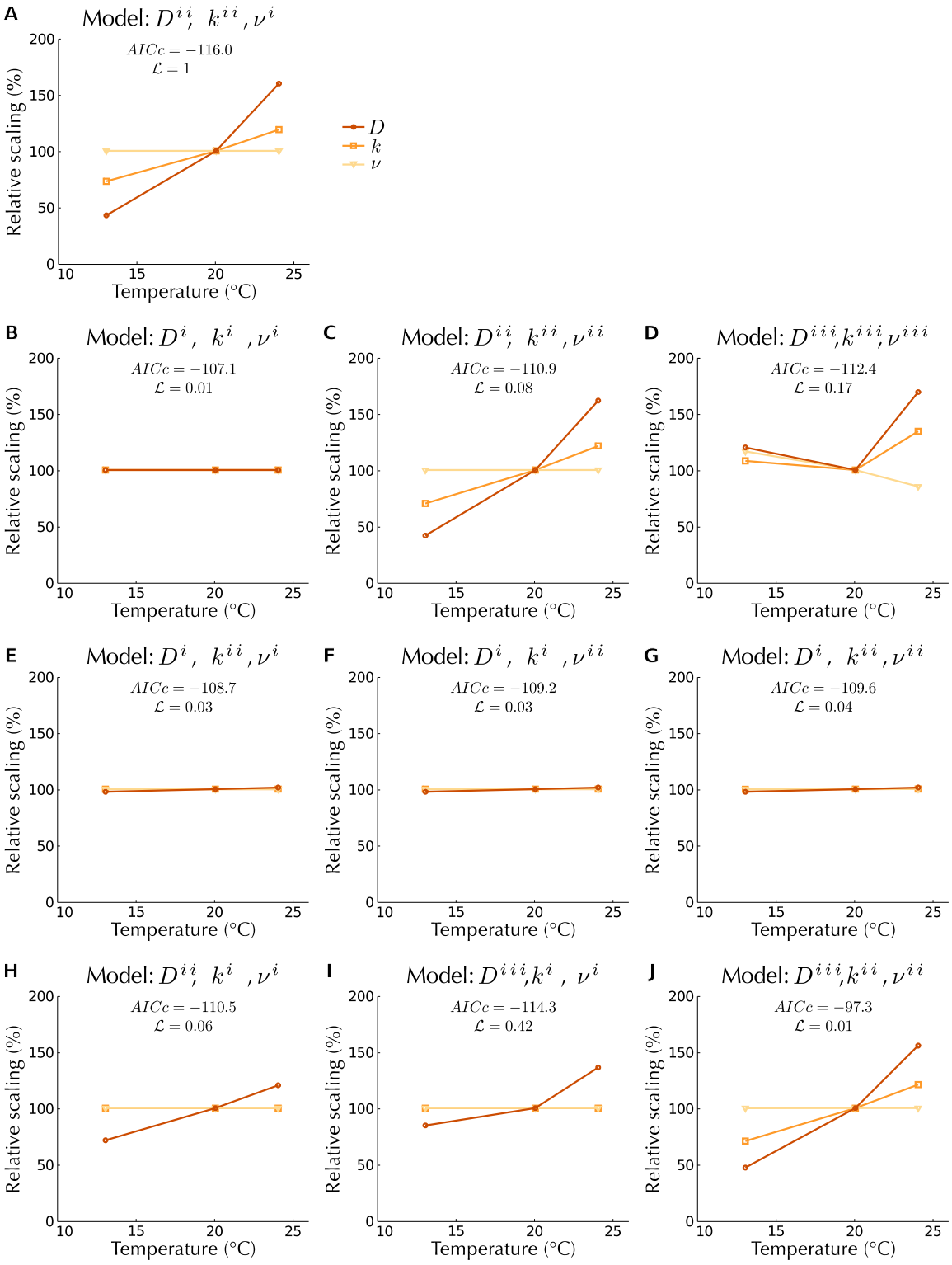

- **Figure S11**. Diffusion and biochemical reaction rates have Arrhenius-like kinetics while flows are temperature invariant. Relative value of the coefficients at the different temperatures, for diffusion (D, circles and dark ochre line), reaction rates (k, squares and

ochre) and cortical flows (ν, triangles and light ochre) for temperature independent models (constant rates, *i*), Arrhenius temperature dependence models (*ii*) or independent values for each temperature (*iii*). Indicated are the performance of each model using the Akaike Information Criterion (AICc) with a correction with the described log-likelihood function (Eq. 1) and the relative likelihood with respect to the highest likelihood model (**A**). All models confirm that diffusion is more sensitive to variations in temperature than biochemical rates (i.e. the dark ochre curve is steeper than the ochre one). In particular, models D^i, in which diffusion is invariant to temperature, restrains the temperature adaptation of both reaction rates and cortical flow (**B, E-G**). Note that in all models, cortical flows are mostly invariant with respect to temperature. In particular, ν^j (**A**) outperforms ν^{ji} (**C**), supporting an apparent compensation mechanism to changes in temperature.

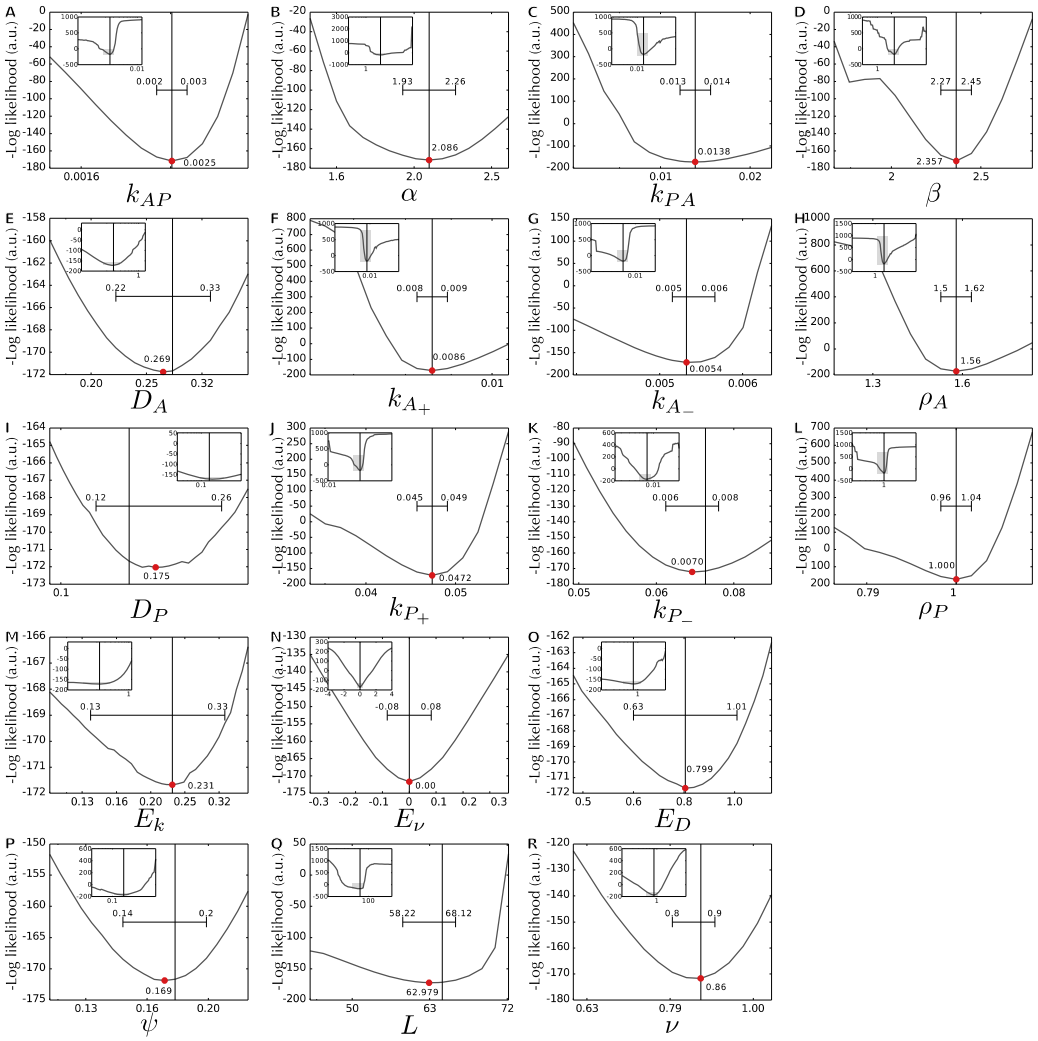

- **Figure S12**. Sensitivity analysis of model M4 with respect to the experimental dataset. This analysis was performed using the model corresponding to Fig. S10 J on the three temperature average kymographs (see Fig. 5 A-C). Each panel displays the value of the negative log-likelihood given a relative change in the value of the indicated parameter. The vertical line indicates the relative default value of the parameter (Tables S1 and S3) and the red dot points at the value corresponding to the highest likelihood score. The horizontal bar delimits the 95% confidence interval overlaid with the corresponding absolute parameter value. The inset shows the full range of variation while the larger panel magnifies the area around the confidence interval (shaded in gray). (**A-D**) Optimized unmeasured parameters of the mutual inhibition terms. Note that the best value for α (**B**, red dot) was not reached because a simulation cannot be initialized with this value; instead a default initialization value was used in this analysis. (**E-L**)

Remaining parameters of the model. (**M-O**) Parameters of the temperature adaptation terms. Note that E_ν is perfectly symmetric because the absolute value of the activation energies are used. (**P-Q**) Dimension parameters of the cell. (**R**) Scaling factor for the cortical flows.

Supporting References

1. Abràmoff, M., P. Magalhães, and S. Ram. 2004. Image processing with ImageJ. Biophotonics Int. 11: 36–42.
2. Amer, A., and E. Dubois. 2005. Fast and reliable structure-oriented video noise estimation. IEEE Trans. Circuits Syst. Video Technol. 15: 113–118.
3. Blanchoud, S., Y. Budirahardja, F. Naef, and P. Gönczy. 2010. ASSET: a robust algorithm for the automated segmentation and standardization of early *Caenorhabditis elegans* embryos. Dev. Dyn. an Off. Publ. Am. Assoc. Anat. 239: 3285–96.
4. Goldstein, B., and S.N. Hird. 1996. Specification of the anteroposterior axis in *Caenorhabditis elegans*. Development. 122: 1467–74.
5. Rappleye, C. a, A. Tagawa, R. Lyczak, B. Bowerman, and R. V Aroian. 2002. The anaphase-promoting complex and separin are required for embryonic anterior-posterior axis formation. Dev. Cell. 2: 195–206.
6. Bellman, R. 1952. On the theory of dynamic programming. Proc. Natl. Acad. Sci. U. S. A. 38: 716–9.
7. Goehring, N.W., P.K. Trong, J.S. Bois, D. Chowdhury, E.M. Nicola, et al. 2011. Polarization of PAR proteins by advective triggering of a pattern-forming system. Science. 334: 1137–41.
8. 2010. NIST Handbook of mathematical functions. In: Olver FWJ, DW Lozier, RF Boisvert, CW Clark, editors. New York, NY: Cambridge University Press.
9. Goehring, N.W., C. Hoege, S.W. Grill, and A.A. Hyman. 2011. PAR proteins diffuse freely across the anterior-posterior boundary in polarized *C. elegans* embryos. J. Cell Biol. .
10. Hansen, N., and A. Ostermeier. 2001. Completely derandomized self-adaptation in evolution strategies. Evol. Comput. 9: 159–95.
11. Lagarias, J.C., J.A. Reeds, M.H. Wright, and P.E. Wright. 1998. Convergence properties of the Nelder--Mead simplex method in low dimensions. SIAM J. Optim. 9: 112–147.
12. Filzmoser, P., R. Maronna, and M. Werner. 2008. Outlier identification in high dimensions. Comput. Stat. Data Anal. 52: 1694–1711.
13. Munro, E., J. Nance, and J.R. Priess. 2004. Cortical flows powered by asymmetrical contraction transport PAR proteins to establish and maintain anterior-posterior polarity in the early *C. elegans* embryo. Dev. Cell. 7: 413–24.
14. Jaqaman, K., D. Loerke, M. Mettlen, H. Kuwata, S. Grinstein, et al. 2008. Robust single-particle tracking in live-cell time-lapse sequences. Nat. Methods. 5: 695–702.
15. Olivo-Marin, J.-C. 2002. Extraction of spots in biological images using multiscale products. Pattern Recognit. 35: 1989–1996.
16. Smith, C.S., N. Joseph, B. Rieger, and K. a Lidke. 2010. Fast, single-molecule localization that achieves theoretically minimum uncertainty. Nat. Methods. 7.
17. Niwayama, R., K. Shinohara, and A. Kimura. 2011. Hydrodynamic property of the cytoplasm is sufficient to mediate cytoplasmic streaming in the *Caenorhabditis elegans* embryo. Proc. Natl. Acad. Sci. U. S. A. 108: 11900–5.

18. Tseng, Q., E. Duchemin-Pelletier, A. Deshiere, M. Balland, H. Guillou, et al. 2012. Spatial organization of the extracellular matrix regulates cell-cell junction positioning. Proc. Natl. Acad. Sci. U. S. A. 109: 1506–11.
19. Kawai, M., T. Kido, M. Vogel, R.H. a Fink, and S. Ishiwata. 2006. Temperature change does not affect force between regulated actin filaments and heavy meromyosin in single-molecule experiments. J. Physiol. 574: 877–87.
20. Laidler, K.J. 1985. Chemical kinetics and the origins of physical chemistry. Arch. Hist. Exact Sci. 32: 43–75.
21. Dell, A.I., S. Pawar, and V.M. Savage. 2011. Systematic variation in the temperature dependence of physiological and ecological traits. Proc. Natl. Acad. Sci. U. S. A. 108: 10591–6.
22. Doremus, R.H. 2002. Viscosity of silica. J. Appl. Phys. 92: 7619.
23. Hird, S.N. 1996. Cortical actin movements during the first cell cycle of the *Caenorhabditis elegans* embryo. J. Cell Sci. 109: 525.
24. Cheeks, R.J., J.C. Canman, W.N. Gabriel, N. Meyer, S. Strome, et al. 2004. *C. elegans* PAR proteins function by mobilizing and stabilizing asymmetrically localized protein complexes. Curr. Biol. 14: 851–62.
25. Mayer, M., M. Depken, J.S. Bois, F. Jülicher, and S.W. Grill. 2010. Anisotropies in cortical tension reveal the physical basis of polarizing cortical flows. Nature. .
26. Bieler, J., C. Pozzorini, and F. Naef. 2011. Whole-embryo modeling of early segmentation in *Drosophila* identifies robust and fragile expression domains. Biophys. J. 101: 287–96.